Real-fluid phase transition in cavitation modelling considering dissolved non-condensable gas

Songzhi Yang, Chaouki Habchi

Real-fluid phase transition in cavitation modelling considering dissolved non-condensable gas

Songzhi Yang (杨松枝)[1,2], Chaouki Habchi*[1,2]
[1]IFP Energies Nouvelles, 1 et 4 Avenue de Bois-Préau, 92852 Rueil-Malmaison, France
[2]Institut Carnot IFPEN Transports Energies, 1 et 4 Avenue de Bois-Préau, 92852 Rueil-Malmaison, France

Abstract

In this article, a fully compressible two-phase flow model combined with a multi-component real-fluid phase equilibrium solver is proposed for the cavitation modelling. The model is able to simulate the dissolving process of non-condensable gas through resolving the real-fluid phase change equations. A three-dimensional cavitating nozzle test is considered to validate the suggested model. The achieved numerical results have been compared to available X-ray experiments. The results have confirmed that the model can tackle the phase transition phenomena including gas dissolving and homogeneous nucleation processes. Thus, the cavitation inception has been modelled dynamically when the fluid crosses the phase boundary from single-phase state to two-phase state and vice-versa. The effects of non-condensable gas on the cavitation inception, development and unsteadiness have been particularly analysed, based on the Large-Eddy simulations and X-ray experiments. Finally, the encountered challenges are mentioned, aiming at providing recommendations for similar researches.

Keywords: two-phase flow model; real fluid; dissolved gas; cavitation, phase equilibrium

*Corresponding author, Email: chaouki.habchi@ifp.fr

1 **NOMENCLATURE**

P	Pressure	T	Temperature
P_c , T_c	Critical pressure, temperature	R	Universal gas constant
z_k, Y_k	Molar fraction, mass fraction of each species (k)	x_k, y_k	Liquid, vapor phase mole fraction of species (k)
ω	Acentric factor	$\boldsymbol{\omega}$	Vorticity
v	Molar volume (m^3/mol)	u	Molar internal energy (J/mol)
ρ	Density (kg/m^3)	e	Molar internal energy (J/kg)
ψ_v	Vapor molar fraction	Y_k	Mass fraction of each species
α_g, α_l	Volume fraction of gas, liquid	V_i	Velocity (m/s)
C_s	Speed of sound (m/s)	$C_{s,g}, C_{s,l}$	Speed of sound in the gas phase, liquid phase (m/s)
$\alpha_p \rho_{p,k}$	Specific density of component k in phase p (kg/m^3)	$k_{i,j}$/ BIP	Binary interaction parameter
M_w	Molar weight (kg/mol)	Pr	Prandtl number
μ	Dynamic viscosity (kg/(m*s))		
Superscripts			
n	Numerical values in current time step	,	Temporary numerical values during the iteration process
L, T	Laminar/turbulent	C	Numerical results after the flow solver or Phase C
Subscripts			
k	Species index	g	Gas phase
l	Liquid phase	p	Phase index
Abbreviations			
PR EoS	Peng-Robinson equation of state	TP flash	Isothermal-Isobaric flash
UV flash	Isoenergetic-Isochoric flash	HTHP	High temperature high pressure
DIM	Diffused interface model	HEM	Homogeneous Equilibrium Model
HRM	Homogeneous Relaxation Model	VOF	Volume of fluid
LS	Level-set	EoS	Equation of state
3D	Three-dimensional		

2

1. Introduction

Cavitation is the development of vapor bubbles in a flowing liquid. It is triggered as the local static pressure drops to the fluid saturated value. This phenomenon may happen in hydraulic devices such as hydro-turbines, propellers, pumps or fuel injectors [1]–[4]. This study is mainly focused on but not limited to cavitation in injectors. For internal combustion engines, the important effects of in-nozzle cavitation on the fluid velocity, discharge coefficient, as well as on the ensuing fuel-air mixing, engine performance and emission pollutants have been widely recognized and studied [5]–[9].

The most direct cavitation investigation strategy is through experimental observations which is generally based on the transparent optical configurations (nozzles, chambers, etc). The progress of experimental techniques, from the qualitative laser-sheet and shadowgraph techniques [10], [11], to the quantitative X-ray computed tomography techniques [12], [13], and even more recent X-ray radiography [14], [15], have significantly facilitated the observations of the in-nozzle cavitation. Meanwhile, cavitation modelling and simulation also play a key complementary role in the verification of experimental results, which is also the main strategy adopted in this study.

As for the modelling of dispersed phase (bubble or droplet), the numerical models involved can be classified into two categories: the Eulerian continuum approach and the Lagrangian discrete approach. The first approach may be a single-fluid homogeneous model or a multi-fluid model. The widely employed single-fluid Homogeneous Equilibrium Model (HEM) [8], [16]–[18] and Homogeneous Relaxation Model (HRM) [19], [20] have demonstrated excellent performance in predicting cavitating flows. More complicated two-fluid model can describe the liquid and vapor phase simultaneously with individual mass, momentum and energy in each cell as studied in [21]–[23]. In the alternative discrete Lagrangian approach, the vapor phase is usually treated as the dispersed phase or nuclei state with the prescribed diameter and number distributions, as demonstrated in previous works [13], [24], [25].

Besides, depending on the method of locating the interface, the interface tracking models such as Level-Set (LS) and VOF (fluid volume) [9], [26], or the diffuse interface model (DIM) [21], [27], may be used.

In current study, the continuous single-fluid two-phase flow diffused interface model (DIM) is adopted. As a thermodynamic closure for the flow model, a real fluid cubic equation of state (EoS) is employed in order to investigate the effect of real flow properties on phase transition in cavitation modelling with the consideration of dissolved non-condensable gas. In recent years, the real fluid EoS has been widely

employed in the two-phase flow simulation, especially for the high pressure injection [28]–[30]. However, the scenario of cavitation simulation with real fluid equation of state is still extremely scarce for its high thermodynamically and numerical complexities. Indeed, introducing the real fluid EoS into the cavitation modelling enables us to take into account more real and practical physical phenomena, for example the process of gas dissolving and relief from liquid. The widely used EoS like Stiffened-gas EoS [31]–[35], Tait EoS [36] have shown excellent performance in the cavitation modelling in previous studies. Nevertheless, the above mentioned EoSs are not able to address the aforementioned gas dissolving physics, especially bubbles inception. As a matter of fact, cavitation bubbles also contain non-condensable gas that diffuses into them from the liquid where it is present as dissolved gas. Therefore, both liquid and gas phases are multi-component when using real fluid thermodynamics and Vapor-Liquid-Equilibrium (VLE). Recently, Yu, et al. [37] have developed a multiphase compressible model in which the vapor, liquid and non-condensable gas phase are simultaneously considered. However, the real fluid EoS has been applied only for the gas phase to simulate the cavitation and high-pressure diesel sprays. Thus the gas dissolving process is still neglected in their model. On the other hand, the current model avoids the cumbersome process of prescribing the empirical coefficients for the calculation of cavitation and collapse terms. The validations of the current model applied to flash boiling cases and high temperature, high pressure (HTHP) diesel injection process can be found in our recent studies [30], [38]. One noting point about the employment of cubic EoSs series in the multiphase flow equation is the risks of losing hyperbolicity when entering the spinodal region as discussed by many researchers [27], [32], [39], [40]. However, this risk can be prevented through adopting the composite EoS in which liquid flow and gas flow are described with its independent EoS instead of a mixture EoS [38]. Thus, the validity of the speed of sound in the two phase region is sustained by the mixing of each individual positive speed of sound in the liquid phase and vapor phase through the Wood formula [41]. This strategy is adopted in current study.

The research interest in this paper stems from the recent X-ray radiography experiments [42], [43] in which an extra cavitation cloud was observed in the center line of the orifice where the pressure is slightly higher than the saturation value of the fuel as demonstrated in Figure 1 (non-degassed fuel represents the standard fuel). This cavitation cloud appeared in the center line has diminished significantly as decreasing the initial non-condensable gas amount in the fuel as illustrated in Figure 1 (degassed fuel).

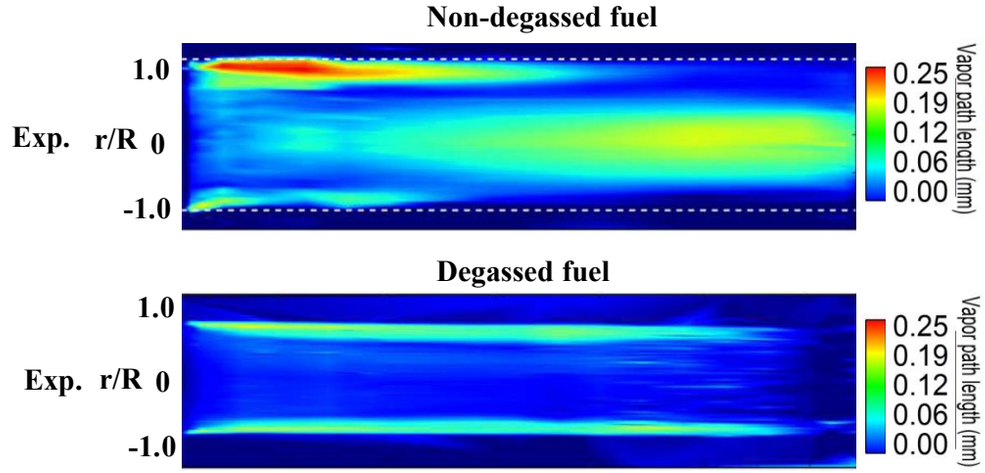

Figure 1 Contour plots of the time-averaged void fraction from the X-ray radiography measurements. The experiment is conducted with a plastic nozzle. These experimental images are republished with permission of Begell house, from 'Duke, Daniel J., et al. "X-Ray Radiography Measurements of Cavitating Nozzle Flow." *Atomization & Sprays* 23.9(2013):841-860.', permission conveyed through Copyright Clearance Center, Inc. The configuration of the geometry is illustrated in Figure 6.

The ensuing numerical results from Battistoni et al. [20] with the HRM model again confirm that the void zones are significantly decreased in the center line as the non-condensable gas amount is reduced in the fluid. However, the latest X-ray radiography experimental measurements from Duke, et al. [15] (Figure 2) about the effect of dissolved gas on cavitation have questioned the previous experimental and numerical findings.

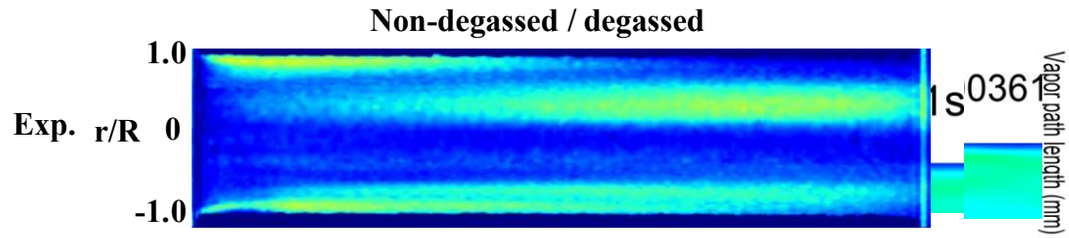

Figure 2 Contour plots of the time-averaged void fraction from the X-ray radiography measurements. The experiment is conducted with the beryllium alloy nozzle. Only one image is displayed since very similar results are obtained using the non-degassed (standard) fuel and degassed fuel. The experiment image is reprinted with permission of SAGE Publications, Ltd, from 'Duke, Daniel J., et al. "X-Ray Radiography of Cavitation in a Beryllium Alloy Nozzle." International Journal of Engine Research, vol. 18, no. 1–2, Feb. 2017, pp. 39–50' copyright ©2020. The configuration of the geometry is illustrated in Figure 6.

They have attributed the void zone in the center line appeared in the earlier experiment [42] (Figure 1, non-degassed case) to the existence of defects on the wall of plastic nozzle, which acts as potential heterogeneous nucleation sites. In contrast,

fewer defects are detected in the beryllium nozzle surface used more recently in [15], leading to very similar experimental averaged results using the non-degassed (standard) and degassed fuels (Figure 2). The significant deviations between these two experimental results (Figure 1 vs. Figure 2) have brought in more uncertainty about the understanding of the effect of dissolved gas on cavitation, which thereby has motivated the current numerical study.

There are also abundant studies concerning the effect of non-condensable gas on spray pattern and engine efficiency [44]–[48]. However, the investigations of the effect of non-condensable gas on cavitation are still limited. Battistoni et al. [20] has employed the HRM model to simulate the in-nozzle cavitation in which the non-condensable gas term is treated as the third phase in addition to the liquid and vapor phases. One noting point is that the non-condensable gas phase in their model is seen as free gas which cannot be dissolved into the liquid and is therefore not participating in the phase change process. Whilst with current real fluid phase equilibrium model proposed below, the non-condensable gas can be dissolved into the liquid and is indeed able to experience phase transition, which may promote the fuel evaporation. As a matter of fact, once the phase transition is triggered, this denotes the non-condensable gas has been through the nucleation process, first and before the fuel as it is generally the most volatile.

In the work of Zhang et al. [49], they demonstrated experimentally that the dissolved oxygen has minor effect on the length of cavitation in a Venturi tube. Amini et al. [50] investigate the incipience and completion thresholds of tip vortex cavitation in a hydrofoil with varied amount of dissolved gas through experimental observations. They found that the tip vortex cavitation incepts at lower pressure as the dissolved amount gas is reduced and disappears at much higher pressure in the fully saturated water. Gireesan and Pandit [51] have used the diffusion limited model to study the influence of the CO_2 and Argon (Ar) mixture on the cavitation and find that the bubble grows larger and the intensity of collapse decreases as CO_2 composition is increased. In general, it is found that the studies of the non-condensable gas are closely linked with the nucleation rate, cavity generation rate, bubble collapse intensity, surface tension and other chemical properties.

The research here is devoted to shedding some light on the understanding of the effect of dissolved gas on the in-nozzle cavitation phenomena using a real fluid EoS. The main difference with previous models lies in the method of dealing with gaseous and vaporous cavitation. In current study, both cavitation regimes can be simulated with the thermodynamics equilibrium model [52]. However, the non-condensable gas part involved in previous cavitation modelling [19], [20] has been treated as free gas instead of dissolved gas. In fact, in the current model described below, the dissolved

gas is modelled as a part of the liquid phase and its dissolution (or separation) from liquid is closely linked with the homogeneous nucleation phenomenon.

This paper has been organized as followings: first, the mathematics descriptions about the two-phase flow model and thermodynamics solver are briefly recalled. More detailed descriptions can be found in our previous work [38][53]. Next, the numerical results of the three-dimensional (3D) simulations of a real size cavitating nozzle are reported along with a detailed analysis. The conclusions part describes the main findings and challenges of the current work.

2. Mathematical model

2.1 Fully Compressible two-phase flow DIM model

The governing equation adopted in current study is a fully compressible multicomponent two-phase flow four-equation model. This system is obtained from the classical two-phase flow non-equilibrium 7-Equation model [54] with the assumption of mechanical and thermal equilibrium. As formulated in the following Eqs.(2.1)-(2.4), the four-equation model includes the mass balance equations for different species (index: k) in the gas (index: g) and liquid (index: l) phases (Eqs.(2.1)-(2.2)), mixture momentum (Eq.(2.3)), and mixture specific internal energy (Eq.(2.4)), respectively.

$$\frac{\partial \alpha_l \rho_{l,k}}{\partial t} + \frac{\partial \alpha_l \rho_{l,k} V_i}{\partial x_j} = \dot{m}_{l,k} \tag{2.1}$$

$$\frac{\partial \alpha_g \rho_{g,k}}{\partial t} + \frac{\partial \alpha_g \rho_{g,k} V_i}{\partial x_j} = \dot{m}_{g,k} \tag{2.2}$$

$$\frac{\partial \rho V_i}{\partial t} + \frac{\partial \rho V_i V_j}{\partial x_i} = \frac{\partial P}{\partial x_i} + \frac{\partial \tau_{ij}^{L,T}}{\partial x_i} \tag{2.3}$$

$$\frac{\partial \rho e}{\partial t} + \frac{\partial \rho e V_i}{\partial x_i} = -P\frac{\partial V_i}{\partial x_i} - \frac{\partial q_i^{L,T}}{\partial x_i} + \tau_{ij}^{L,T}\frac{\partial V_i}{\partial x_j} \tag{2.4}$$

The right hand side (RHS) terms of $\dot{m}_{l,k}$ and $\dot{m}_{g,k}$ are mass exchanging rate in the liquid and vapor phases, respectively, restricted by $\dot{m}_{l,k}$+ $\dot{m}_{g,k}$ = 0. $\tau_{ij}^{L,T}$ is the shear stress tensor covering the laminar (L) and turbulent (T) contributions, formulated as $\tau_{ij}^{L,T} = \tau_{ij}^{L} + K_0\tau_{ij}^{T}$ with $K_0 = 1$ for turbulent flows. As described in our previous studies [21], [38], a standard Boussinesq approximation is used for the modelling of

$\tau_{ij}^{L,T}$ in which the turbulent viscosity is given by the simple subgrid-scale Smagorinsky model. Whereas, the laminar viscosity is computed from Chung's equation, referring to [55], [56]. In Eq.(2.4), e represents the specific internal energy; $q_i^{L,T}$ is the heat conduction flux, modelled as $q_i^{L,T} = -\lambda \frac{\partial T}{\partial x_i}$ based on Fourier's law. The heat conduction coefficient λ contains the laminar and turbulent contributions. The laminar contribution is computed from Chung's correlation and the turbulent one is estimated with the constant Prandtl number ($Pr_t = 0.9$). α_p denotes the volume fraction of phase p which is computed in the phase equilibrium solver along with $\dot{m}_{p,k}$. One salient point about the current model lies in the consideration of the nucleation and dissolving process of the non-condensable gas which is realized with the real-fluid phase equilibrium model. The liquid phase is indeed a multi-component system including both fuel and dissolved non-condensable gas. In most previous cavitation models, only the gas phase is usually considered as multi-component, and the liquid phase is assumed as single component [9], [20]. In current equation system, the mass transferring between the liquid and gas phase is computed in Vapor-Liquid-Equilibrium (VLE) solver for each component (see Section 2.2.2). Thereby the number of mass transport equation is 2* N (N denotes the number of species). The employment of real fluid EoS in each phase also facilitates the consideration of compressibility and other related physics, especially for the pure liquid phase and two-phase mixtures.

2.2 Real fluid phase equilibrium solver

2.2.1 Equation of state

To realize the free dissolving and dissolution of the non-condensable gas, as well as considering the thermal effect during cavitation, a non-linear real fluid equation of state has been selected in current study. With the ideal compromise of computational efficiency and accuracy, Peng Robinson (PR) EoS (Eq.(2.5)) is chosen to describe the relation between P, v and T. As aforementioned, the studies of cavitation modelling with real fluid EoS are still limited. For instance, Yu et al. [37] has recently applied the PR EoS to take into account the thermal effects for in-nozzle cavitation modelling under high injection pressure conditions. However, the dissolved gas effect is still neglected in their study. In the current modelling approach, both phases (the liquid and gas phases) are described with the PR EoS (Eq.(2.5)) linked through the phase equilibrium assumption. For each phase the mixing of different species is realized by the van der Waals mixing rule (Eq.(2.6)).

$$P = \frac{RT}{v-b} - \frac{a(T)}{v(v+b)+b(v-b)} \tag{2.5}$$

Where, $a(T) = 0.45724\frac{R^2{T_c}^2}{P_c}\alpha(T)$, $b = 0.07780\frac{RT_c}{P_c}$, $\alpha(T) = (1+m(1-\sqrt{T_r}))^2$

$$m = 0.37464 + 1.5422\omega - 0.26992\omega^2$$

R denotes the universal gas constant. P_c and T_c represent the critical pressure and temperature values for single component and ω denotes the acentric factor.

van der Waals mixture rules are formulated as follows,

$$\begin{gathered} a = \sum\sum x_i * x_j * a_{ij} \\ a_{ij} = (1-k_{ij})(a_i * a_j)^{0.5} \\ b = \sum x_i * b_i \end{gathered} \tag{2.6}$$

x_i is the molar fraction of each component. k_{ij} denotes the binary interaction parameter which is generally fitted based on the experimental data.

2.2.2 Phase change model

The critical phase change phenomena (evaporation, condensation) during the cavitation modelling are realized with a multicomponent vapor-liquid equilibrium (VLE) model which is constructed based on the assumption that liquid and vapor phase reach equilibrium instantaneously within each simulation time step. No constraint is set for the time-scale of relaxation to equilibrium with current model compared to the Homogeneous Relaxation Model (HRM) [14]. All the fluid states including the pure liquid phase, pure vapor phase and the vapor-liquid coexisting state can be dynamically simulated using the proposed model.

The right hand side terms ($\dot{m}_{l,k}$, $\dot{m}_{g,k}$) calculation and closure of the flow system (Eqs.(2.1) -(2.4)) are realized by building the relation between internal energy (e), density (ρ), mass fraction (Y_k) and pressure (P), temperature (T), known as the UV flash process [57][38]. First, with the direct unit transformation, molar internal energy (u) and molar volume (v) can be obtained directly from (e) and (ρ) using molar weight M_w, as shown in Eq.(2.7). The molar internal energy (u) is computed with the ideal gas part (u_0) and the departure part (u_d) (given by Eq.(2.8)). The ideal gas internal energy is obtained with the empirical coefficient correction equation referred to [58]. The departure function is formulated as Eq.(2.9) according to the PR EoS. The density (ρ) or specific volume (v) is computed directly by solving the cubic equation [59]. Unlike the explicit relation between internal energy (u) and temperature (T) as in SG EoS [32], [33], an iterative algorithm is necessary to find P, T from u, v and z_k (molar fraction of the species) with the cubic EoS. Before initiating the UV flash iteration process, the initial molar fraction of species (z_k^c) in the two-phase mixture, the quasi-steady or non-equilibrium phase compositions (liquid phase and vapor phase: x_k^c, y_k^c) and the vapor mole fraction (ψ_v^c) in the liquid-vapor mixture can be computed from the specific densities ($\alpha_p^c \rho_{p,k}^c$) by using Eqs.(2.10)-(2.11). Here, the superscript c denotes the values obtained from the flow solver at the end of Phase C (see Section 2.2.3 and

particularly Figure 3).Then, the solving procedures are continued with the determination of flow state as shown in the algorithm summarized in Table 1. Since the (P^{n+1}, T^{n+1}) for next cycle are not known as a prior, the (P^n, T^n) from previous cycle are used as the initial guess to perform the stability test [38], [53]. This method is valid based on the fact that the time step is small between two flow solver cycles. Once the flow state is ascertained, an iterative procedure is necessary to obtain the final (P^{n+1}, T^{n+1}). During the iteration, the molar internal energy and molar volume (denoted u_{mix} and v_{mix}) are updated with the properties of each phase Eq.(2.12). One noting point is that in the case of single phase, the phase composition x_k^{n+1}, y_k^{n+1} and molar vapor fraction ψ_v^{n+1} are assumed to be the same as the values of x_k', y_k' and ψ_v' obtained by the flow solver. Generally, the opposed phase in the single-phase situation is seen as the trifle phase. Eventually, the new specific density $\alpha_p^{n+1}\rho_{p,k}^{n+1}$ are calculated with Eq.(2.13) using the volume fraction (α_p^{n+1}) and the final molar volume of species in each phase obtained from PR EoS. The speed of sound (Cs^{n+1}) is then computed with the Wood formula written as Eq.(2.14). Since the mixture speed of sound in the two-phase state is computed with the mixing of the independent speed of sound in each phase, this can effectively avoid the unphysical negative speed of sound. Thereby, the hyperbolicity of the flow balance equation system (Eq.(2.1)-(2.4)) is thus ensured, as discussed in [38]. More detailed descriptions about the thermal solver can be found in recent publications [38], [53].

$$u = e * M_w, v = \frac{M_w}{\rho} \tag{2.7}$$

$$\boldsymbol{u = u_d + u_0} \tag{2.8}$$

$$\boldsymbol{u_d = \frac{T\frac{da}{dT} - a}{2\sqrt{2}b} ln(\frac{v + (1+\sqrt{2})b}{v + (1-\sqrt{2})b})} \tag{2.9}$$

Table 1 Algorithm of UV flash

Algorithm 1 Update P^{n+1}, T^{n+1}, Cs^{n+1}, $\alpha_p^{n+1}\rho_{p,k}^{n+1}$ from e^c, ρ^c, $\alpha_p^c\rho_{p,k}^c$, P^n, T^n
STEP 0 Compute u^c, v^c, ψ_v^c, z_k^c, x_k^c, y_k^c from e^c, ρ^c, $\alpha_p^c\rho_{p,k}^c$ using Eqs.(2.7), (2.10)-(2.11)
STEP 1 Verify Initial flow state based on (u^c, v^c, z_k^c) and (P^n, T^n, z_k^c) through stability test.
STEP 2 If the flow state is stable as single phase, a direct iteratively searching for the updated (P', T') with Newton algorithm based on PR EoS is performed with the initial quasi-steady phase composition (x_k^c, y_k^c) and vapor fraction (ψ_v^c). Here assign $x_k' = x_k^c$, $y_k' = y_k^c$, $\psi_v' = \psi_v^c$.
STEP 3 If the flow state is unstable, an iteratively searching for the updated P', $T'$with Newton algorithm is performed with the continuous updating of phase composition (x_k', y_k') and vapor fraction (ψ_v') based on phase split computation in the inner loop. (see Ref.[38] for the involved algorithm)
STEP 4 Update P^{n+1}, T^{n+1}, Cs^{n+1}, $\alpha_p^{n+1}\rho_{p,k}^{n+1}$ from x_k', y_k', ψ_v' by using Eqs.(2.13)-(2.14) and Eq.(2.5)

$$\boldsymbol{z_k} = \frac{(\sum_p \boldsymbol{\alpha_p \rho_{p,k}})\boldsymbol{M_{w_{mix}}}}{(\sum_{p,k} \boldsymbol{\alpha_p \rho_{p,k}})\mathbf{M_{w_k}}},\ \boldsymbol{Y_k} = \frac{(\sum_p \boldsymbol{\alpha_p \rho_{p,k}})}{(\sum_{p,k} \boldsymbol{\alpha_p \rho_{p,k}})} \tag{2.10}$$

$$\boldsymbol{x_k} = \frac{\boldsymbol{\alpha_l \rho_{l,k} M_{wl}}}{\sum_k (\boldsymbol{\alpha_l \rho_{l,k}}) * \boldsymbol{M_{w_k}}},\ \boldsymbol{y_k} = \frac{\boldsymbol{\alpha_g \rho_{g,k} M_{wg}}}{\sum_k (\boldsymbol{\alpha_g \rho_{g,k}}) * \boldsymbol{M_{w_k}}},\ \boldsymbol{\psi_v} = \frac{(\sum_k \boldsymbol{\alpha_g \rho_{g,k}})\boldsymbol{M_{wmix}}}{\boldsymbol{\rho M_{wg}}} \tag{2.11}$$

M_{w_k} denotes the molar weight of species (k). M_{w_g}, M_{w_l} represent the average molar weight of gas phase and liquid phase, respectively. $\rho_{p,k}$ represents the partial density of species k in phase p.

$$\begin{gathered} \boldsymbol{u_{mix}} = \boldsymbol{\psi_v} * \boldsymbol{u_g} + (\mathbf{1} - \boldsymbol{\psi_v}) * \boldsymbol{u_l} \\ v_{mix} = \psi_v * v_g + (1 - \psi_v) * v_l \end{gathered} \tag{2.12}$$

$$\begin{gathered} \rho = \frac{M_w}{v},\ \rho = \alpha_g \rho_g + \alpha_l \rho_l, \\ \alpha_g = \psi_v * \frac{v_g}{\psi_v * v_g + (1 - \psi_v) * v_l}, \text{ with } \alpha_l = 1 - \alpha_g \end{gathered} \tag{2.13}$$

$$\frac{1}{\rho_{mix} C_{s,mix}^2} = \frac{\alpha_g}{\rho_g C_{s,g}^2} + \frac{\alpha_l}{\rho_l C_{s,l}^2} \tag{2.14}$$

2.2.3 Coupling of flow solver with phase change model

In this Section, the coupling procedure between the thermodynamics solver and the flow solver is elucidated to enhance the understanding of the main implementation stages. In IFP-C3D [60], the transport equations (mass, momentum, energy balance equations) are solved sequentially from Phase A, Phase B, Phase C Phase D based on a time-splitting numerical scheme, as illustrated in Figure 3. The solver includes the flow solver and thermodynamics solver. The flow solver covers three stages namely, Phase A, Phase B and Phase C. First, after the initialization ($t = t^0$), the contribution of possible Lagrangian spray and combustion source terms may be computed in Phase A. Therefore, Phase A stage is not pertinent for the current flow system (Eqs.(2.1) - (2.4)). In the following Phase B stage, usually called "Lagrangian phase", the Navier-Stokes equations are solved without the convection terms and the pressure, temperature and velocity are updated implicitly with the SIMPLE numerical scheme[61], including a BICGSTAB and SOR preconditioners [60]. Then, the grid cell boundaries are mapped back to their original position (in the absence of wall movement) in Phase C (also called "Eulerian stage"). The transport variables including mass, energy and momentum from Phase B are updated in Phase C using a quasi-second order upwind (QSOU) explicit numerical scheme. The Minmod slope limiter is used for scalar fluxes, and Van Leer slope limiter is used for momentum fluxes (see [60]). No phase change is considered in these three stages. The thermodynamic solver is implemented in the final stage, Phase D. With the known internal energy (e^c), density (ρ^c) and specific density ($\alpha_p^c \rho_{p,k}^c$) from phase C, the new temperature (T^{n+1}),

pressure (P^{n+1}), phase compositions (x_k^{n+1}, y_k^{n+1}) and speed of sound (Cs^{n+1}) need to be calculated for ending the current time-step (or cycle). This procedure is attributed to the phase change model as described in Section 2.2.2. In phase D, the occurred evaporation or condensation phenomenon corresponds to the generation and collapse of bubbles during cavitation. One noting point is that there is no fluid flowing in or out of Phase D which means the flow is frozen in this stage. In fact, the phase equilibrium solver based on PR EoS has corresponded to the relaxation of pressure, temperature and the Gibbs energy terms in the original 7-Equation model [21]. Since the liquid and gas phases are both resolved as multicomponent system, the involved gas phase or dissolved gas in the liquid phase constitutes the main physical novelty compared to previous researches using SG-EoS for instance [21], [62], [63].

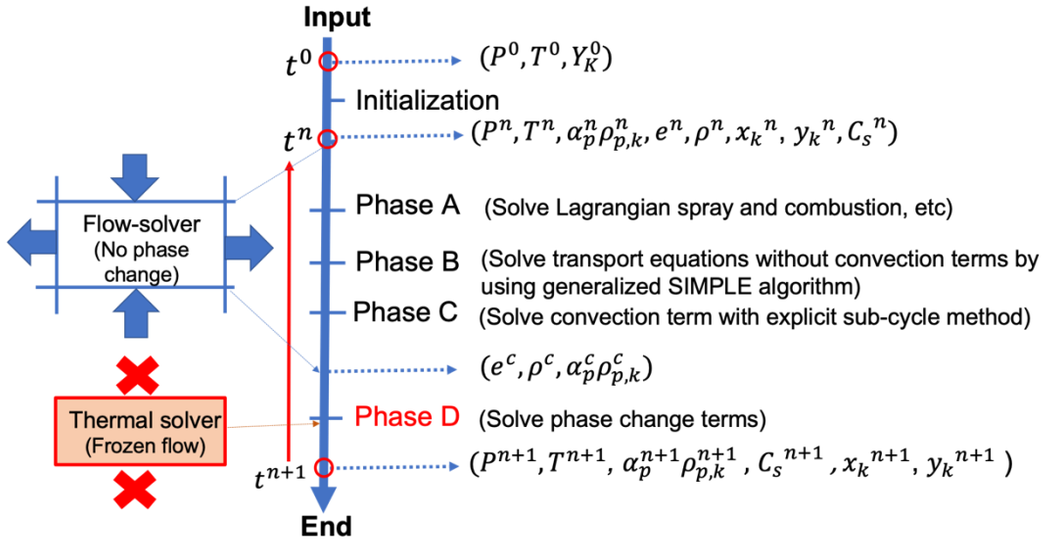

Figure 3 Illustration of coupling between the thermodynamic solver and flow solver in IFP-C3D

3. 3D cavitating nozzle simulation

Firstly, a thermodynamics study of the effect of non-condensable gas (N_2) on the phase change behaviour is conducted. Then the simulation results of a 3D cavitating nozzle along with a detailed analysis of cavitation inception, nucleation and turbulence are reported. The fuel used for cavitation modelling in this study is gasoline calibrated fluid (Viscor 16BR) referring to the relevant experiments [15], [42]. Since the real fluid EoS is employed, the involved input parameters like critical points and acentric factor have referred to the properties of n-decane.

3.1 Thermodynamics study of the effect of non-condensable gas on phase change

To investigate the thermodynamic equilibrium behaviour of Viscor and N_2 system, the method that is generally utilized at given temperature and pressure is the isothermal flash computation (TP flash) as noted in STEP 3 (Table 1). An important variable to represent the generated vapor at phase equilibrium calculation is the vapor mole fraction, (ψ_v). This parameter indicates the overall amount of vapor which includes the vaporized fuel and the gaseous N_2 that was dissolved in the liquid phase. Figure 4 (a) illustrates the evolution of ψ_v with the amount of N_2 within the pressure range of 1 bar to 10 bar. As shown in Figure 4, one may see that the total vapor amount ψ_v has increased with the addition of N_2 in the feed. This implies the compressed fuel initially containing a high amount of N_2 will promote cavitation inception (or homogeneous nucleation). Some researcher has validated this phenomenon with experiments [64], in which they have attributed the intensifying of cavitation to the increase of cavitating nuclei coming from the dissolved gas. The dissolved gas can help decrease the energy needed to form a bubble and reduce the tensile strength of the fluid. One noting point in Figure 4 is that at each pressure, there exists a transition point where the ψ_v is changing from a negative value to the positive one which actually denotes the gas has transformed (or transitioned) from the dissolved state to the free gas in the bubble. To some extent, this may indicate the initial formation of a nuclei. The negative vapor fraction implies no vapor is generated in the flow and the amount of nitrogen is actually fully dissolved inside the liquid phase. In other words, the fluid is in single liquid phase until a certain mole fraction of N_2 is reached according to the pressure and temperature conditions. Meanwhile, the phase state has been through the transition from pure liquid to two-phase. In addition, with higher pressure, the N_2 concentration needed for phase transition (or nucleation) also increases notably which proves that high pressure can dissolve more N_2. The exponential growth trend of molar fraction in the liquid phase (dissolved N_2) with pressure is shown in Figure 4 (b).

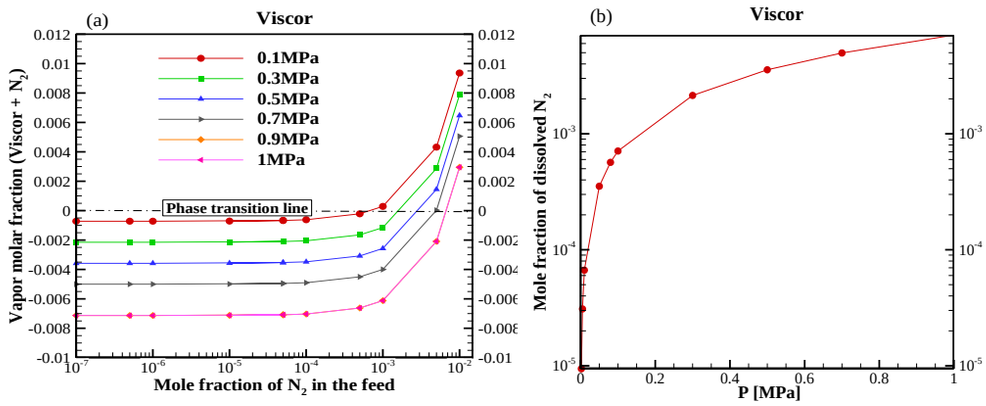

Figure 4 (a) The variation of vapor mole fraction with the molar fraction of N_2 at T = 293 K; P = 1-10 bar. (b) The evolution of dissolved amount of N_2 with the pressure increasing from 0.01 bar to 10 bar.

It is well-known that cavitation incepts as the pressure drops to the saturation value. Thus, saturation pressure is an important index to indicate the inception of cavitation. The evolutions of saturation pressure with temperature for n-dodecane (n-$C_{12}H_{26}$) and Viscor fuels at different N_2 concentrations are illustrated in Figure 5. The saturation pressure of pure n-$C_{12}H_{26}$ computed with PR EoS has been compared to the reference data from NIST [65] (Figure 5 (a)). As observed in this Figure, an excellent agreement has been achieved at the temperature range of 300 K-600 K for pure n-$C_{12}H_{26}$. In addition, the saturated pressure of the mixture system is approaching the pure component value as the N_2 mass fraction (Y_{N2}) is less than 2E-6. However, obvious deviations are detected as Y_{N2} is increased to 2E-6. These deviations are more evident at low temperature (~300 K) conditions. A significant increase of saturation pressure is witnessed as Y_{N2} climbs from 2E-6 to 2E-3. A similar trend is also detected for the Viscor fuel (Figure 5 (b)). Minor differences are found for the saturation pressure as the N_2 concentration is between 2E-6 and 2E-7 for Viscor. Since larger saturation pressure corresponds to higher N_2 concentration, this will facilitate the inception of cavitation as confirmed in the following 3D simulation.

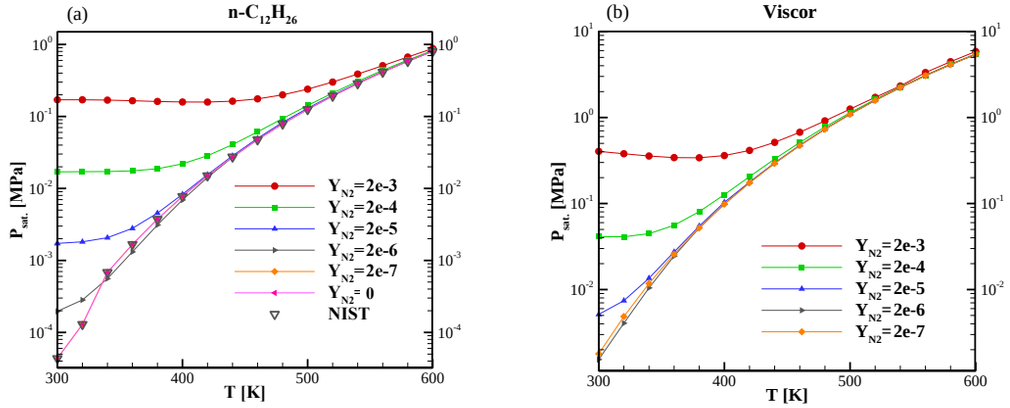

Figure 5 (a, b) illustrate the variation of saturation pressure for n-dodecane and Viscor systems at a temperature range of 300 K-600 K with different N_2 concentrations. Y_{N2} denotes the mass fraction of N_2.

3.2 Simulation setup

In this section, the fully compressible two-phase flow model based on phase equilibrium theory is applied to simulate the cavitation phenomenon in a 3D real size nozzle. The working fuel is gasoline calibrated fuel (Viscor 16BR) as noted above.
The involved non-condensable gas is N_2. The simulation results are compared to available experimental data based on X-ray phase contrast imaging [66] and X-ray radiography measurement [15]. The detailed numerical parameters are summarized in Table 2.

Table 2 Numerical parameters for the cavitation simulations

Simulation models	Fully compressible two-phase flow model
Cavitation model	Real fluid multi-component phase equilibrium solver
Initial N_2 mass fraction	Non-degas: 2E-5; Degas: 2E-6
Turbulence model	Large Eddy Simulation with Smagorinsky subgrid scale model
Grid type	Hexahedral
Minimum mesh resolution	5 μm
Time integration	First order
Spatial discretization	Secondary order
Boundary Conditions	Pressure inlet, P_{inlet} : 1 MPa; Temperature T_{inlet} : 293 K; $Y_{n2,inlet}$: 2E-5, 2E-6; Pressure outlet, P_{outlet} : 0.1 MPa
Time step	2E-10 - 4E-10, CFL: 0.2
Initial nozzle condition	Submerge state, T: 293 K, P: 0.1 MPa,V: 0 m/s

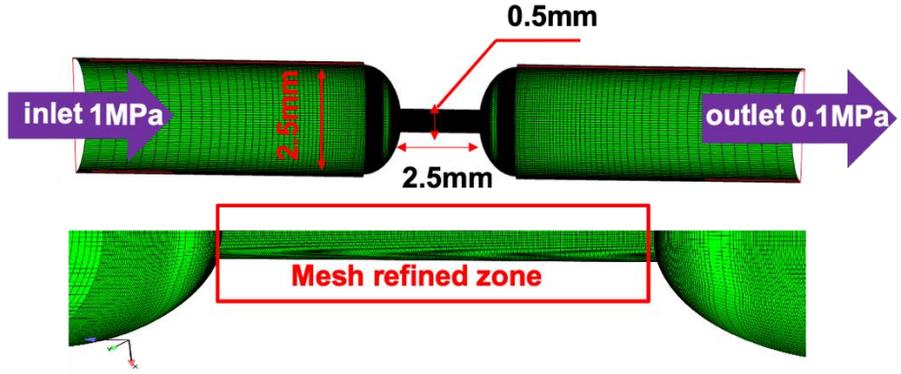

Figure 6 Configuration of $1/2$ geometry and mesh refining zone with a total of 560425 cells and the minimum grid resolution is 5 μm. The diameter of the orifice is 0.5 mm and its length is 2.5mm [15]**. The fluid flows from the left inlet to the right outlet with the pressure gradient of 1MPa to 0.1 MPa.**

The configuration of the nozzle is illustrated in Figure 6. The diameter of the orifice is 500 μm. Detailed descriptions can be found in Ref. [15]. Due to the limited computational resource, only half of the geometry is simulated. There are around 64 cells across the orifice diameter which corresponds to an average cell size of 7.84 μm. The refined mesh zones are distributed inside the orifice, the inlet and outlet regions, as shown in Figure 6.

Since the original experiments are performed in the submerged conditions [42][15], the simulation also assumes the initial conditions in the nozzle to be full of liquid with a trifle amount of N_2, as summarized in Table 2. The inlet and outlet are set with pressure boundary conditions with the 10 bar and 1 bar, respectively, close to the experimental conditions [42][15].

Besides, as discussed in the Introduction, in the original experiments, the tested conditions have contained the degassed and non-degassed conditions. Since no exact quantified amount of N_2 is identified in the fluid during experiments, it is essential to determine a critical value to differentiate the non-degassed situation from the degassed state, for the convenience of modelling. As shown in Figure 4(a), the fluid state has transformed from single liquid state to two-phase saturation state with the increase of N_2 in the fluid mixture. As the fluid is still in pure liquid state, N_2 is therefore fully dissolved in the fluid, and the trifle N_2 amount is exactly the same as the amount of dissolved N_2. Two initial values for the mass fraction of N_2, Y_{N2} equalling to (2E-5, 2e-6) are selected to represent the non-degassed and degassed state, respectively. The amount of N_2 in the non-degassed state is the same as the work of Battistoni [20]. In contrast, the N_2 concentration in the degassed state setting with 2E-6 is slightly higher than previous work (2E-7 in [20]) because in the current study, N_2 is in the dissolved state unlike in [20] conditions where N_2 is instead in the free gas state.

All the cavitation simulations are conducted with a finite volume scheme within the large eddy simulation framework. The involved sub-grid scale (SGS) model for the turbulence is the Smagorinsky model.

3.3 Model assessment against X-ray Radiography data

The original experiments [42][15] have been conducted under the non-degassed and degassed conditions with the nozzle made of different materials (plastic, metal). Obvious differences are found for the results obtained with these different materials. As discussed in the Introduction, an extra void cloud is only detected with the plastic nozzle under the non-degassed situation [42](Figure 1). The effect of dissolved N_2 is proven to be extremely weak when the metal nozzle is used [15](Figure 2). According to Duke et al. [42][15], the extra void zone is formed because of local imperfections (or roughness) on the plastic nozzle surface.

For the simulated cases Y_{N2} = (2E-5, 2E-6), the following analysis is based on a limited computational time: 0.36 ms and 0.44 ms, respectively. Although both cases have not reached the quasi-steady flow, the following comparisons with the experiments based

on the latest time instants have proved to be appropriate, particularly near the hole entrance and the orifice wall where the cavitation is the most intense. Therefore, the following discussions will focus on the model assessment against X-ray phase contrast imaging and X-ray Radiography data. However, because of the nozzle made of different materials (plastic, metal) and also the fact that initial Y_{N2} is unknown in the experiments, the comparison of the numerical results with experiments can only be qualitative.

It is also noteworthy that considering the compressibility of the liquid and gas mixtures, our model has improved the speed accuracy of traveling waves in the computational domain between the inlet and outlet, but these waves have led to longer CPU time to reach steady state compared to previous studies [20].

The numerical results are calculated based on the integrated void fraction (α_g) along the cast ray for both cases, the same as in the X-ray experiments. The line of sight integrations are performed in the $Y(0^\circ)$ direction as well as the rotated X (90°) direction, as illustrated in Figure 7. One noting point is that the experimental images relating to the X-ray integrated void fraction are the time-averaged results collected at the steady flow state. Therefore, it is not appropriate to compare the instantaneous LES contour to the averaged experimental images shown in Figure 1 and Figure 2. Instead, the instantaneous X-ray phase contrast images from the experiments [42], [66] are displayed to compare with the simulated contour, as shown in Figure 8 and Figure 9, respectively. It is evident to observe from Figure 9 that the model can accurately capture the main cavities in the entrance and along the wall for both cases. In the experiments, because of the effect of defects in the plastic nozzle surface, more cavities are detected for the case with dissolved gas as marked in the circle in Figure 8 [66]. It seems that the dissolved gas adhering to the surface of defects has functioned as nuclei for the extra cavitating zones.

As for the numerical results, the cavitation structure and behaviours have proved to be very different in the degassed and non-degassed cases. First, the cavitation in the degassed case is much more intense than in the non-degassed case. In addition, it is more fragmented and dispersed for the degassed case which may be attributed to stronger waves unsteadiness and turbulence as shown in the following discussions.

However, such dispersed cavitation is not detected in the experimental results. But surprisingly, the steady cavitation structure in the experimental degassed case has presented some resemblance with the numerical non-degassed case. Therefore, the real amount of non-condensable gas in the experiments is probably far exceeding the adopted values (2E-5 and 2E-6) in this work. Yet, the obtained numerical results for the non-degassed case has proved to be quantitatively close to the X-ray experimental data, as discussed below.

Since only half geometry is simulated in this work, the radiography results for the other half nozzle have been obviously assumed the same as the simulated half-nozzle.

Thus, the numerical radiography results shown in Figure 9 in the $Y(0^\circ)$ direction are

computed (then doubled) accordingly. On the other hand, the radiography contour for the non-simulated half-nozzle in the X (90°) direction is also taken as the symmetry of the simulated results in Figure 9. Besides, in the X(90°) direction, the line of sight integration path covers the whole nozzle. Therefore, in this case, the numerical radiography results depicted in Figure 9 are post-processed in a more straightforward manner. As shown in Figure 9, the inlet sharp corner cavitation can be captured correctly with current LES simulations. Whereas, affected by unsteadiness and turbulence, the cavitation is not evenly distributed in the 0° and 90° directions, for both N_2 concentration cases. With limited computational time, the void distribution seems not fully extended to the exit of the orifice for the non-degassed case. However, the cavitating flow is very close to the steady state.

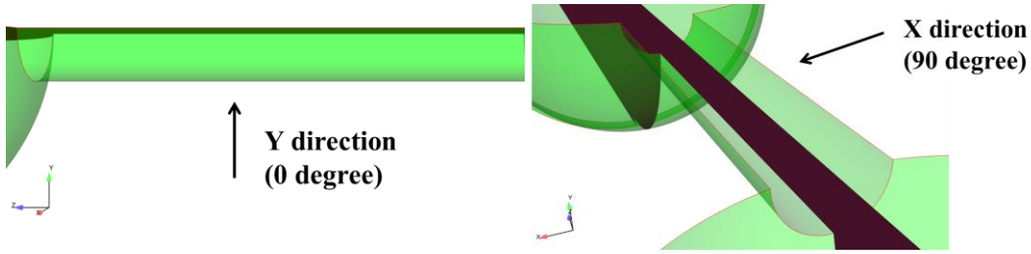

Figure 7 Demonstration of numerical radiography projection direction. *X* direction denotes the rotated view based on the *Y* direction.

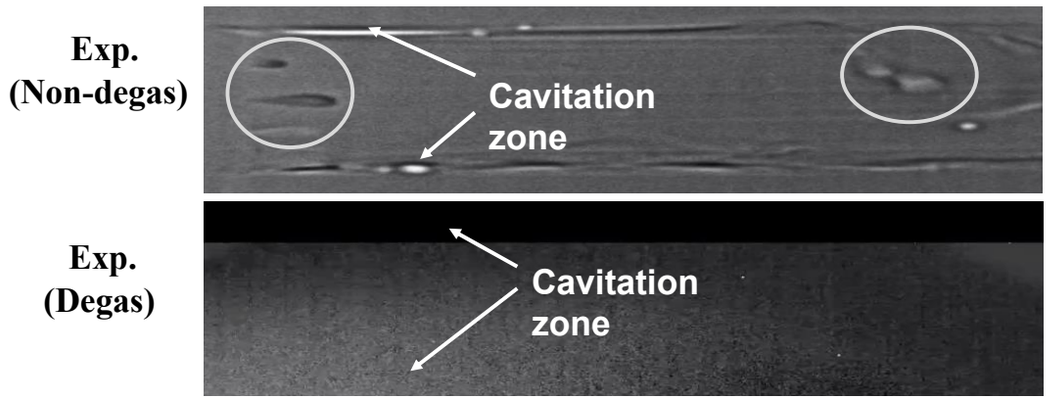

Figure 8 Instantaneous X-ray phase contrast images relating the cavitating nozzle performed with the non-degassed fuel and degassed fuel. The experimental images are snapped directly from the video in the website [67] **with permission of Argonne National Laboratory. The wall cavitation is in the bright zones as illustrated by the arrows. The cavities marked in the circles are induced by the defects of the nozzle. The flow is from left to right.**

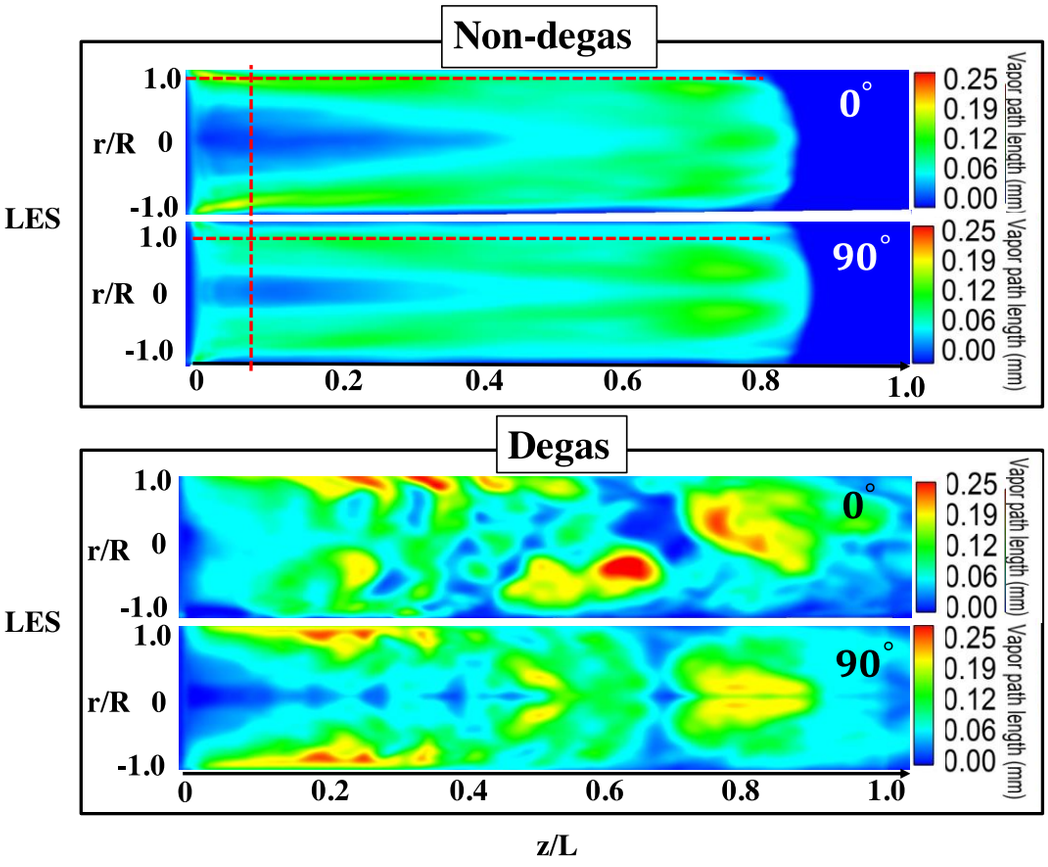

Figure 9 Contour plots of the numerical radiography based on the line of sight integration of volume fraction of gas (α_g) for the non-degassed case ($Y_{N2} = 2E-5$, t = 0.36 ms) and degassed case ($Y_{N2} = 2E-6$, t = 0.44 ms). The 0° view and 90° view denote the radiography are along X and Y direction, respectively. The fluid is from left to right.

As aforementioned, since the numerical results of the non-degassed case show high resemblance to the experimental results qualitatively, a further quantitative comparison with the latest experimental results is conducted to assess the numerical model. Two profiles of void fraction have been plotted in the locations near the hole entrance and close to the orifice wall (see dashed lines in Figure 9) where the cavitation is most intense. More precisely, the radial profiles are at the axial distance of $^{z}/_{L}$ = 0.1 (z is the axial distance from hole inlet and L is the length of the hole) and the axial profiles are plotted along the wall of the orifice at ($^{r}/_{R}$ = 0.99) (r is the radial distance and R is the hole radius). To ensure the accuracy of the averaged results, several numerical results are collected around the targeted position within a deviation of 0.05 mm. As it may be observed in Figure 10, the numerical axial and radial profile shapes follows the experimental results well, but these are somewhat overestimated in the near wall for the 0° direction integration and underestimated for the 90° direction. Therefore, the averaged value of the two directions corresponds better to

the averaged experimental profiles, as depicted in Figure 10. The uneven distribution of the void fraction as aforementioned can be observed both in axial and radial directions. It is undeniable that averaging the LES results based on longer computational time as well as realizing the spatial averaging (through computing the entire geometry) would better highlight the correspondence with the averaged experimental results. This will be confirmed in future work.

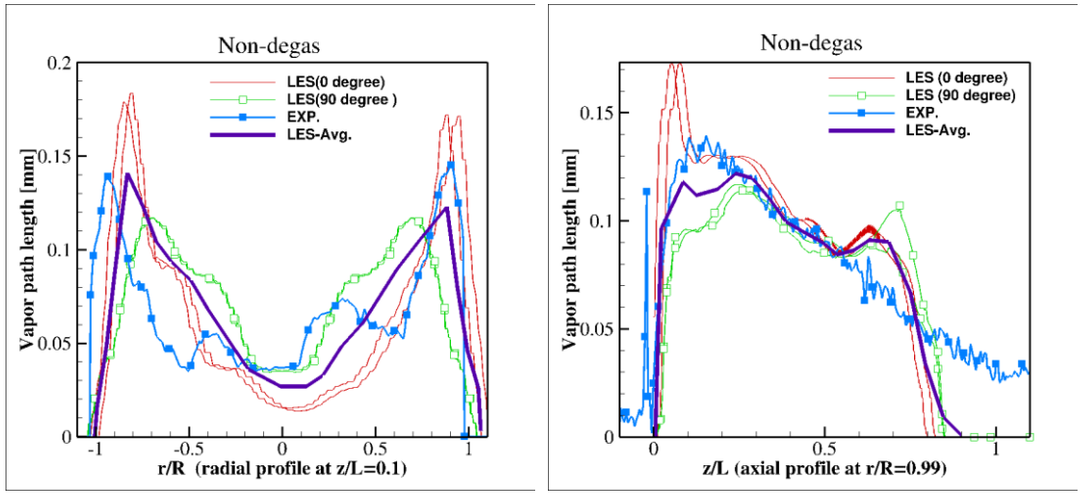

Figure 10 Quantitively comparison between the averaged radiography experimental data [15] **and the LES results for the non-degassed case ($Y_{N2} = 2E-5$, t = 0.36 ms).**

3.4 Effect of N_2 on cavitation inception

As discussed in the previous Section 3.1, higher N_2 concentration in the fluid will bring about the elevation of vapor pressure and the reduction of tensile strength for the cavitation inception. Therefore, one may expect that the cavitation will incept earlier in the case with more N_2. Indeed, as displayed in Figure 11, where the cavitation zone is shown with the iso-surface (α_g = 0.5), the cavitation in the case with higher amount of N_2 ($Y_{N2} = 2E-5$) starts at earlier time, around 260 μs, than in the case with less N_2 ($Y_{N2} = 2E-6$) for which the inception of cavitation is severely lagged up to around 310 μs.

The minimum pressure is also larger for the fluid with more N_2 at the location of cavitation inception, as shown in the palette of Figure 11. Hence this result is consistent with the fact that vapor pressure increases with higher amount of nitrogen, as discussed previously in Section 3.1. One noting point is that the cavitation has not appeared in the inlet corner of the orifice for both cases. Instead, it starts in the shear stress layer as shown in the velocity contour in Figure 12. This phenomenon has been confirmed in recent experimental observation [68]. As a matter of fact, the cavitation has incepted at the position of Z/L = 0.1 where the pressure clip-planes are depicted in Figure 11. Then, the formed nuclei are transported downstream with the flow.

Meanwhile, more regions start cavitating. It is interesting to detect that with similar time interval (20 μs) in Figure 11, the cavity formation and growth rate is much larger for the flow with higher amount of N_2, as observed at the time interval [260 μs, 280 μs], compared to the time interval [310 μs, 330 μs]. This implies that the dissolved gas promotes the growth rate of the bubbles in addition to facilitating the inception of bubbles nuclei. With more non-condensable gas in the fluid, the maximum velocity proved to be slightly higher (54 m/s instead of 53 m/s) as shown in the velocity contour (Figure 12).

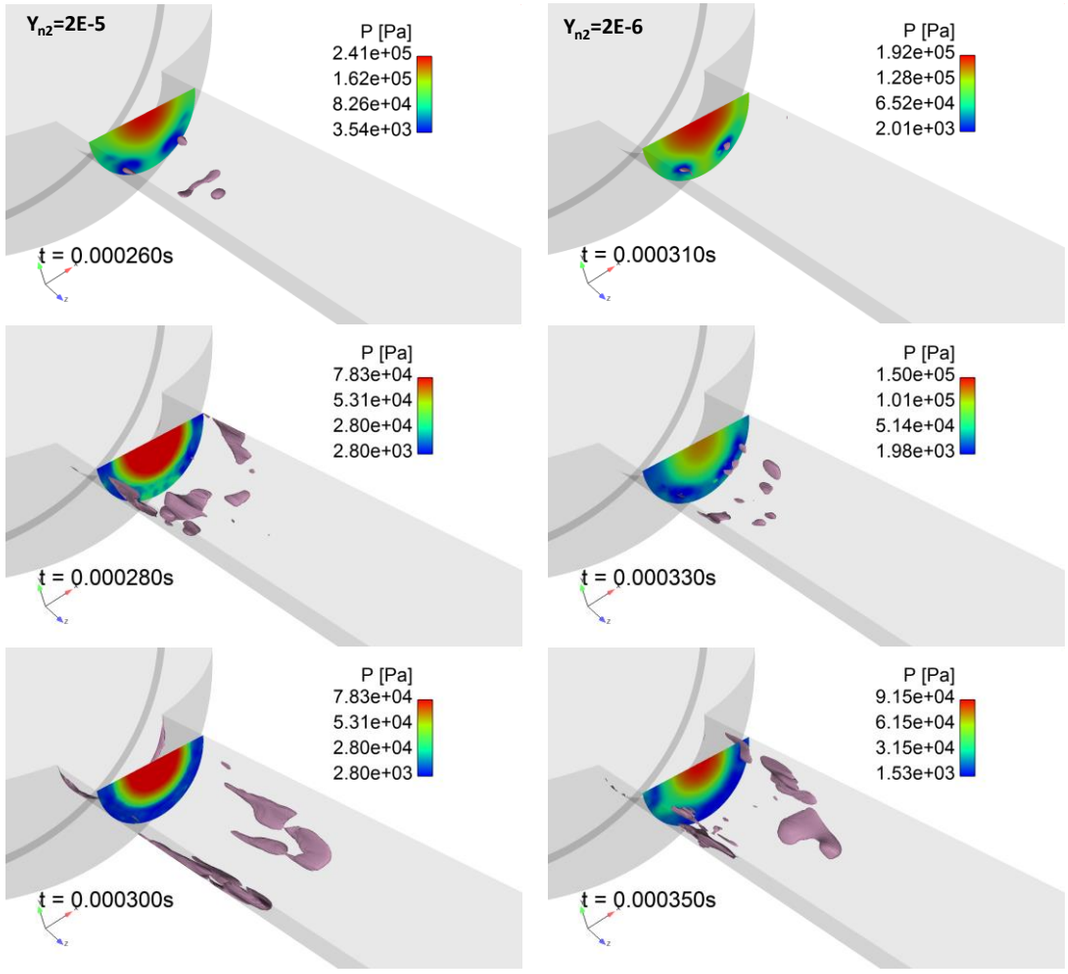

Figure 11 Demonstration of the effect of N_2 on cavitation inception and developing processes. The cavity is presented with the iso-surface of gas volume fraction (α_g= 0.5). The left and right column of images corresponds to the Case Y_{N2} = 2E-5 and Case Y_{N2} = 2E-6, respectively.

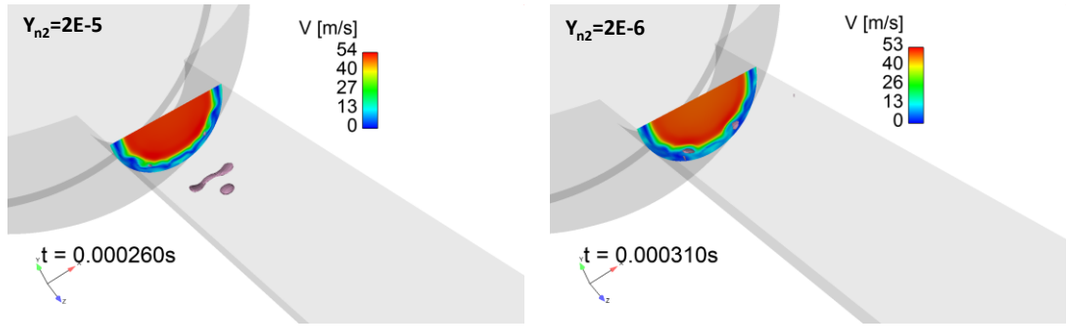

Figure 12 Demonstration of the effect of N_2 on the velocity contour at the location of cavitation inception. The left, right column of images corresponds to the Case Y_{N2} = 2E-5 and Case Y_{N2} = 2E-6, respectively.

3.5 Effect of N_2 on cavitation evolving

With the phase equilibrium model developed in this work, the detailed analysis of the homogeneous nucleation process becomes possible when the capillary effect is neglected. Indeed, the current test cases have demonstrated the process of phase transition from a multicomponent (Viscor, N_2) single-phase flow to a two-phase flow inside the orifice, automatically. In this section, phase transition (i.e. nucleation) is discussed further, as it constitutes one of the most important novelties of this work.

The following discussion is based on the degassed case (Y_{N2} = 2E-6). In this case, it is proved that the initial fluid is thermodynamically in single-phase. The phase transition (i.e. nucleation) from a single phase (multicomponent liquid) towards a two-phase, then further to a single phase gas state, corresponds to the formation of resolved bubbles, as shown in Figure 13. For instance, the phase transition phenomenon may be observed in this figure while the gas volume fraction (α_g) is increasing progressively up to 1 E-2 during the period (280-320) µs. The initial nuclei keep growing from the fully dissolved N_2 state ($\alpha_g < 1E-4$) to a two-phase situation, and finally to free gas ($\alpha_g \geq 0.99$) with enough long time, as shown in Figure 13. One noting point is the evolution of the volume fraction of the N_2 in the gas cavities ($\alpha_{g,N2}$) which is defined with the formula $\alpha_{g,N2} = \alpha_g * y_{N2}$, where y_{N2} is the molar fraction of N_2 in the gas phase. The N_2 amount in the nuclei has kept increasing and almost 90% of the cavities are filled with N_2 as time evolves to 0.38 ms. However, in the earlier period (280-360) µs, the amount of N_2 is lower than half of the overall gas cavity volume. In the phase equilibrium model, restricted by the constraint $y_{N2} + y_{viscor} = 1$ in gas phase, the evolving of the amount of the vaporous fuel and N_2 are mutually affected, which also implies that the gaseous cavitation and vaporous cavitation processes are mutually impacted. According to the current numerical results, vaporous cavitation is the dominant phase transition process during the nucleation stage. Then, gaseous cavitation becomes more critical during the growth of the cavities. It is therefore undeniable that gaseous cavitation plays a major role in the later stage according to the current results. Another interesting point is that the evolving process has seen the collapse of vaporous bubbles, especially at later stage

as shown in Figure 13 for t > 0.38 ms. In addition, only gaseous (or non-condensable) cavitation seems to survive in the later stage.

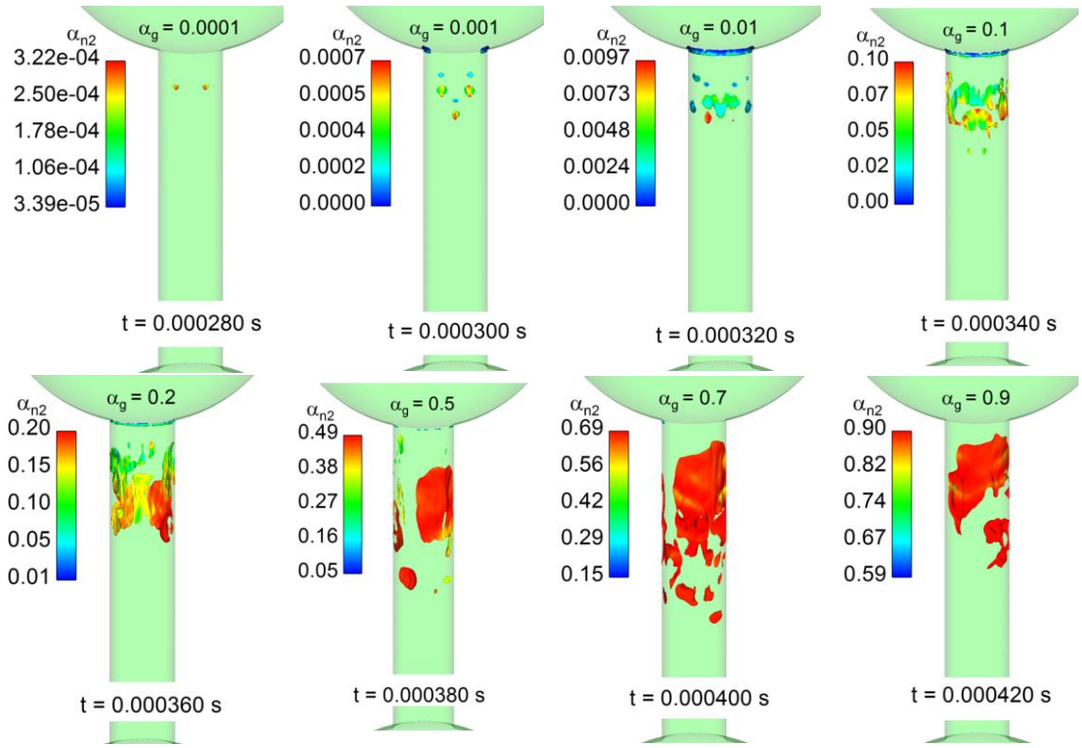

Figure 13 Demonstration of nucleation and cavitating process within the time intervals of 0.14 ms. The cavitating zone is presented by iso-surfaces of different void fraction (α_g) indicated at the top of each image. The iso-surfaces are colored by the amount of gas N_2 in the gas phase ($\alpha_{n2} = \alpha_{g,N2}$), as shown by the different palettes.

3.6 Effect of N_2 on unsteadiness and turbulence

As aforementioned, the case with less non-condensable gas has shown stronger unsteadiness and turbulence compared to the one with more non-condensable gas. This is further clarified in the contour plots of velocity, eddy viscosity and vorticity, as shown in Figure 14. The turbulent viscosity is much larger for the degassed case. More complex vorticity is also detected in this case. The generation of vorticity is attributed to more intense cavitation and collapse, as observed in previous PIV experimental observations [69]. One could also observe the vorticity streaks generated especially at the orifice entrance in the non-degassed case. Indeed, they are very similar to the structures observed experimentally in Figure 8 also for the non-degassed case. In addition, in contrast with the non-degassed case where the flow is relatively smooth, the vorticity and the turbulent eddies are convected downstream but also towards the hole axis, as could be noticed in Figure 14 in degassed case. More intense cavitation is also witnessed for the degassed case which may be again verified by the

smaller density and larger density gradient (Figure 15). In this Figure, a large two-phase region is formed especially in the second half of the nozzle for both non-degassed and degassed cases, which corresponds to the regions with the smallest sound speed. This is witnessing the local Mach number has far exceeded one, which denotes the flow has entered the supersonic regime. This implies that it is important to take into account the compressibility of the liquid for the cavitation simulation which may explain why the stationary state is too long to reach.

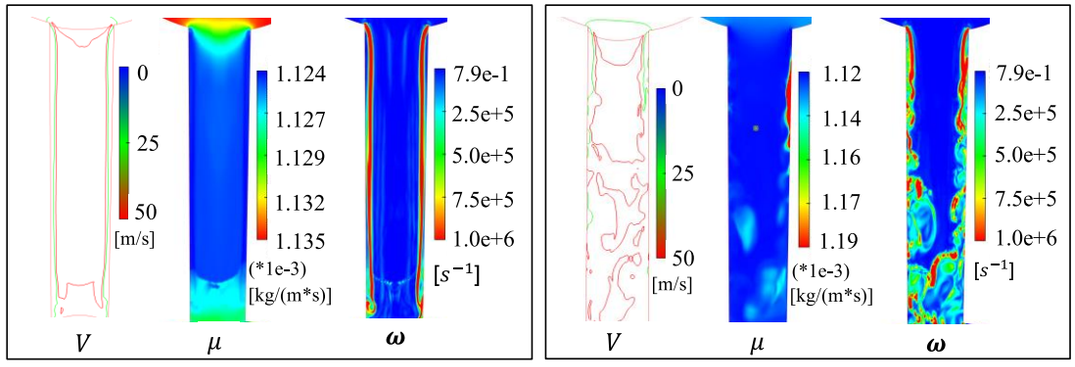

Non-Degassed Degassed

Figure 14 Contour plots of velocity (V), eddy-viscosity (μ) and voticity (ω) for the non-degassed and degassed cases. The clip plane is the symmetry plane of the nozzle geometry normal to Y direction (see Figure 7).

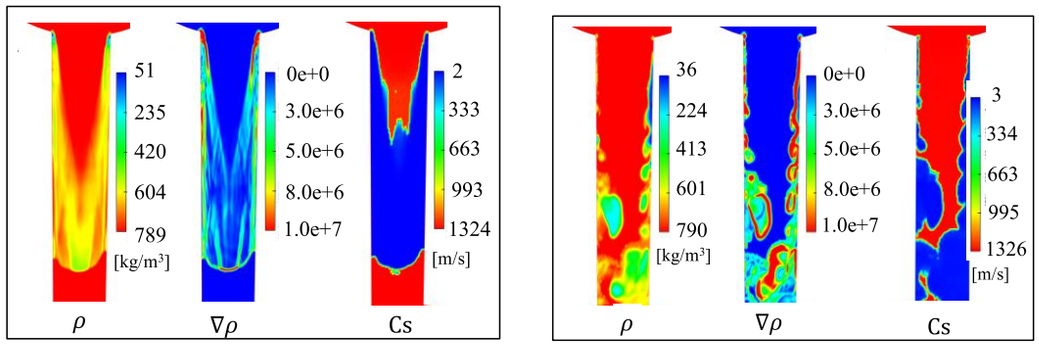

Non-Degassed Degassed

Figure 15 Contour plots of density (ρ), density gradient ($\nabla\rho$) and speed of sound (Cs) for the non-degassed and degassed cases. The clip plane is the symmetry plane of the nozzle geometry normal to Y direction (see Figure 7).

4. Conclusions and challenges

A fully compressible two-phase flow model based on phase equilibrium theory with real fluid equation of state has been described in the current study. The capability of fluid transition from pure liquid to two-phase state has been firstly verified through stand-alone vapor-liquid equilibrium computation. It is shown that with the addition of N_2, the involved non-condensable gas can evolve from the dissolved state to free gas state. Besides, more N_2 can be dissolved at high pressure. Then, the model was applied to simulate the cavitation phenomenon inside a single-hole nozzle to investigate the effect of dissolved N_2 on the cavitation behaviour. The obtained quasi-steady results are quantitatively comparable to the X-ray experimental results. Several conclusions are summarized from the LES simulations:

1) With real-fluid phase equilibrium solver, the model is able to dynamically predict the phase transition process such as the nucleation phenomenon and subsequent cavitation.

2) With more dissolved N_2, the cavitation inception time is much earlier than for degassed fluid.

3) With the formation and collapse of the void cavities, more turbulent unsteadiness is highlighted for the case with less N_2.

The two-phase flow model combined with a real-fluid phase equilibrium solver has been shown to have more advantages in revealing the cavitation physics details than previously published cavitation models using barotropic or incompressible liquid assumptions, for instance. According to the current numerical results, the fraction of non-condensable N_2 in the gaseous cavities have been quantified. It turns out that vaporous cavitation is the dominant phase transition process during the nucleation stage especially in the fluid with minimal N_2. Then, gaseous N_2 cavitation becomes more significant during the growth of the cavities.

Finally, one should admit that there are still several challenges to be addressed for proper cavitation simulations. The first and most important issue is computational efficiency. We found that more than 70% of the CPU time is consumed in the thermodynamic equilibrium computation. A possible solution to address this issue is using tabulation method [70], [71]. Indeed, all the thermal properties including phase composition, speed of sound, internal energy…etc, from phase equilibrium calculation could be stored in a table prepared before the simulation starts. This can avoid the time-consuming thermodynamics computation. The other encountered issue is the convergence problem as approaching the phase boundary. It is found that tons of iterations are needed to reach the convergence criterion at phase boundaries. The main reason is ascribed to the huge gradient of phase properties at the phase

boundary. Potential numerical instabilities caused by the oscillations in the phase boundary are also witnessed. It is recommended to adopt better algorithm to resolve this issue. The current work is expected to provide some references for the cavitation modelling using real-fluid EoS.

Acknowledgement

This project has received funding from the European Union Horizon 2020 Research and Innovation program. Grant Agreement No 675528 for the IPPAD project. The author would like to acknowledge Dr. Daniel Duke for providing the experimental data.

References

[1] P. Koukouvinis, M. Gavaises, J. Li, and L. Wang, "Large Eddy Simulation of Diesel injector including cavitation effects and correlation to erosion damage," *Fuel*, vol. 175, pp. 26–39, 2016.

[2] G. Kähler;, F. Bonelli;, G. Gonnella;, and A. Lamura;, "Cavitation inception of a van der Waals fluid at a sack-wall obstacle," *Phys. Fluids*, vol. 27, no. 123307, 2015.

[3] (张皓晨); H. Z., (左志钢); Z. Z., K. A. Mørch;, and Shuhong Liu (刘树红), "Thermodynamic effects on Venturi cavitation characteristics," *Phys. Fluids*, vol. 31, no. 9, 2019.

[4] P. Koukouvinis, C. Bruecker, and M. Gavaises, "Unveiling the physical mechanism behind pistol shrimp cavitation," *Sci. Rep.*, vol. 7, no. 13994, 2017.

[5] W. H. Nurick, "Orifice Cavitation and Its Effect on Spray Mixing," *J. Fluids Eng.*, vol. 98, pp. 681–687, 1976.

[6] F. Payri, V. Bermúdez, R. Payri, and F. J. Salvador, "The influence of cavitation on the internal flow and the spray characteristics in diesel injection nozzles," *Fuel*, vol. 83, no. 4–5, pp. 419–431, 2004.

[7] M. Blessing, G. König, C. Krüger, U. Michels, and V. Schwarz, "Analysis of Flow and Cavitation Phenomena in Diesel Injection Nozzles and Its Effects on Spray and Mixture Formation," in *SAE Technical Paper Series*, 2010.

[8] C. Habchi, N. Dumont, and O. Simonin, "Multidimensional Simulation of Cavitating Flows in Diesel Injectors By a Homogeneous Mixture Modeling Approach," *At. Sprays*, vol. 18, no. 2, pp. 129–162, 2008.

[9] H. Yu, L. Goldsworthy, P. A. Brandner, and V. Garaniya, "Development of a compressible multiphase cavitation approach for diesel spray modelling," *Appl. Math. Model.*, vol. 45, pp. 705–727, 2017.

[10] H. K. Suh and C. S. Lee, "Effect of cavitation in nozzle orifice on the diesel fuel atomization characteristics," *Int. J. Heat Fluid Flow*, vol. 29, no. 4, pp. 1001–1009, 2008.

[11] C. Badock, R. Wirth, A. Fath, and A. Leipertz, "Investigation of cavitation in real size diesel injection nozzles," *Int. J. Heat Fluid Flow*, vol. 20, no. 5, pp. 538–544, 1999.

[12] D. Bauer, H. Chaves, and C. Arcoumanis, "Measurements of void fraction distribution in cavitating pipe flow using x-ray CT," *Meas. Sci. Technol.*, vol. 23, no. 5, p. 55302, 2012.

[13] E. Giannadakis, M. Gavaises, and C. Arcoumanis, "Modelling of cavitation in diesel injector nozzles," *J. Fluid Mech.*, vol. 616, pp. 153–193, 2008.

[14] D. J. Duke *et al.*, "X-ray radiography measurements and numerical simulations of cavitation in a metal nozzle," in *ILASS Americas 28th Annual Conference on Liquid Atomization and Spray Systems*, 2016, no. May.

[15] D. J. Duke *et al.*, "X-ray radiography of cavitation in a beryllium alloy nozzle," *Int. J. Engine Res.*, vol. 18, no. 1–2, pp. 39-50., 2017.

[16] J. M. Desantes, F. J. Salvador, M. Carreres, and J. Martínez-López, "Large-eddy simulation analysis of the influence of the needle lift on the cavitation in diesel injector nozzles," *Proc. Inst. Mech. Eng. Part D J. Automob. Eng.*, vol. 229, no. 4, pp. 407–423, 2014.

[17] S. Molina, F. J. Salvador, M. Carreres, and D. Jaramillo, "A computational investigation on the influence of the use of elliptical orifices on the inner nozzle flow and cavitation development in diesel injector nozzles," *Energy Convers. Manag.*, vol. 79, pp. 114–127, 2014.

[18] DELANNOY Y., "Two Phase Flow Approach in Unsteady Cavitation Modelling," in *Cavitation and Multiphase Flow Forum*, 1990.

[19] M. Battistoni, S. Som, and D. E. Longman, "Comparison of Mixture and Multifluid Models for In-Nozzle Cavitation Prediction," *J. Eng. Gas Turbines Power*, vol. 136, no. 6, p. 061506, 2014.

[20] M. Battistoni, D. J. Duke, A. B. Swantek, F. Z. Tilocco, C. F. Powell, and S. Som, "Effects of Noncondensable Gas on Cavitating Nozzles," *At. Sprays*, vol. 25, no. 6, pp. 453–483, 2015.

[21] C. Habchi, "a Gibbs Energy Relaxation (Germ) Model for Cavitation Simulation," *At. Sprays*, vol. 25, no. 4, pp. 317–334, 2015.

[22] Y. Wang, L. Qiu, R. D. Reitz, and R. Diwakar, "Simulating cavitating liquid jets using a compressible and equilibrium two-phase flow solver," *Int. J. Multiph. Flow*, vol. 63, pp. 52–67, 2014.

[23] A. Alajbegovic, G. Meister, D. Greif, and B. Basara, "Three phase cavitating flows in high-pressure swirl injectors," *Exp. Therm. Fluid Sci.*, vol. 26, pp. 677–681, 2002.

[24] H. Roth *et al.*, "Effect of Multi-Injection Strategy on Cavitation Development in Diesel Injector Nozzle Holes," in *SAE Technical Paper Series*, 2005.

[25] X. Lyu, S. Pan, X. Hu, and N. A. Adams, "Numerical investigation of homogeneous cavitation nucleation in a microchannel," *Phys. Rev. FLUIDS*, vol. 064303, pp. 1–15, 2018.

[26] W. Yuan, J. Sauer, and G. H. Schnerr, "Modeling and computation of unsteady cavitation flows in injection nozzles," *Mec. Ind.*, vol. 2, no. 5, pp. 383–394, 2001.

[27] F. Petitpas, J. Massoni, R. Saurel, E. Lapebie, and L. Munier, "Diffuse interface model for high speed cavitating underwater systems," *Int. J. Multiph. Flow*, 2009.

[28] C.Rodriguez;, A. Vidal;, P. Koukouvinis;, M. Gavaises;, and M.A. McHug;, "Simulation of transcritical fluid jets using the PC-SAFT EoS," *J. Comput. Phys.*, vol. 374, pp. 444–468, 2018.

[29] J. Matheis and S. Hickel, "Multi-component vapor-liquid equilibrium model for LES of high-pressure fuel injection and application to ECN Spray A," *Int. J. Multiph. Flow*, no. October, 2017.

[30] S. Yang, P. Yi, and C. Habchi, "Real-fluid injection modelling and LES simulation of the ECN Spray A injector using a fully compressible two-phase flow approach," *Int. J. Multiph. Flow*, p. 103145, 2019.

[31] C. Habchi, J. Bohbot, A. Schmid, and K. Herrmann, "A comprehensive Two-Fluid Model for Cavitation and Primary Atomization Modelling of liquid jets - Application to a large marine Diesel injector," *J. Phys. Conf. Ser.*, vol. 656, no. 1, 2015.

[32] R. Saurel, P. Boivin, and O. Le Métayer, "A general formulation for cavitating, boiling and evaporating flows," *Comput. Fluids*, vol. 128, pp. 53–64, 2016.

[33] R. Saurel, F. Petitpas, and R. Abgrall, "Modeling phase transition in metastable liquids. pplication to flashing and cavitating flows," *Int. J. Multiph. Flow*, vol. 607, pp. 313–350, 2008.

[34] O. Le Métayer and R. Saurel, "The Noble-Abel Stiffened-Gas equation of state," *Phys. Fluids*, vol. 28, no. 4, pp. 0–33, 2016.

[35] L. M. Olivier, J. Massoni, and R. Saurel., "Élaboration des lois d'état d'un liquide et de sa

vapeur pour les modèles d'écoulements diphasiques," *Int. J. Therm. Sci.*, vol. 43, no. 3, pp. 265–276, 2004.

[36] E. Lauer, X. Y. Hu, S. Hickel, and N. A. Adams, "Numerical modelling and investigation of symmetric and asymmetric cavitation bubble dynamics," *Comput. Fluids*, vol. 69, pp. 1–19, 2012.

[37] H. Yu, L. Goldsworthy, P. A. Brandner, J. Li, and V. Garaniya, "Modelling thermal effects in cavitating high-pressure diesel sprays using an improved compressible multiphase approach," *Fuel*, vol. 222, pp. 125–145, 2018.

[38] P. Yi, S. Yang, C. Habchi, and R. Lugo, "A multicomponent real-fluid fully compressible four-equation model for two-phase flow with phase change," *Phys. Fluids*, vol. 31, no. 2, p. 026102, 2019.

[39] R. Menikoff and B. J. Plohr, "The Riemann problem for fluid flow of real materials," *Rev. Mod. Phys.*, 1989.

[40] R. Saurel and P. Boivin, "Cavitation Instabilities and Rotordynamic Effects in Turbopumps and Hydroturbines," vol. 575, no. January, 2017.

[41] A. B. Wood., *A Textbook of Sound.* 1955.

[42] D. J. Duke, A. L. Kastengren, F. Z. Tilocco, A. B. Swantek, and C. F. Powell, "X-Ray Radiography Measurements of Cavitating Nozzle Flow," *At. Sprays*, vol. 23, no. 9, pp. 841–860, 2013.

[43] D. J. Duke, A. L. Kastengren, A. B. Swantek, K. E. Matusik, and C. F. Powell, "X-ray fluorescence measurements of dissolved gas and cavitation," *Exp. Fluids*, 2016.

[44] M. Karaeen and E. Sher, "SPRAY CHARACTERISTICS OF DIESEL FUEL CONTAINING DISSOLVED CO2 SPRAY CHARACTERISTICS OF DIESEL FUEL," *At. Sprays*, vol. 21, no. 11, 2011.

[45] A. Rashkovan and E. Sher, "Flow pattern observations of gasoline dissolved CO2 inside an injector," *At. Sprays*, vol. 16, no. 6, 2006.

[46] I. Y. Senda J, Hashimoto K and F. H., "CO_2 Mixed Fuel Combustion System for Reduction of NO and Soot Emission in Diesel Engine.," *SAE Trans.*, pp. 471–481, 1997.

[47] A. Xiao, Jin, Zhen Huang, Ma Junjun and Q. Xinqi, "An experimental study on spray transient characteristics in fuel containing CO2," *At. Sprays*, vol. 19, no. 4, 2009.

[48] Z. Huang, Y. Shao, S. Shiga, and H. Nakamura, "Controlling mechanism and resulting spray characteristics of injection of fuel containing dissolved gas," *J. Therm. Sci.*, vol. 3, no. 3, pp. 191–199, 1994.

[49] H. Zhang, Z. Zuo, and S. Liu, "Influence of dissolved gas content on Venturi cavitation at thermally sensitive conditions," in *Proceedings of the 10th International Symposium on Cavitation (CAV2018)*, 2018, pp. 546–550.

[50] A. Amini, M. Reclari, T. Sano, and M. Farhat, "Effect of Gas Content on Tip Vortex Cavitation," in *Proceedings of the 10th International Symposium on Cavitation*, 2018, pp. 322–325.

[51] S. Gireesan and A. B. Pandit, "Modeling the effect of carbon-dioxide gas on cavitation," *Ultrason. - Sonochemistry*, vol. 34, pp. 721–728, 2017.

[52] S. Yang, C. Habchi, P. Yi, and R. Lugo, "Cavitation Modelling Using Real-Fluid Equation of State.," in *Proceedings of the 10th International Symposium on Cavitation(CAV2018)*, 2018.

[53] S. Yang, "Modeling of Diesel injection in subcritical and supercritical conditions," University of Paris-Saclay, 2019.

[54] M. S. Baer and J. W. Nunziato, "A two-phase mixture theory for the deflagration to detonation (DDT) transition in reactive granular materials," *Int. J. Multiph. Flow*, vol. 12, no. 6, pp. 861–889, 1986.

[55] T. C. Horng, M. Ajlan, L. L. Lee, K. E. Starling, and M. Ajlan, "Generalized Multiparameter Correlation for Nonpolar and Polar Fluid Transport Properties," *Ind. Eng. Chem. Res.*, vol. 27, no. 4, pp. 671–679, 1988.

[56] B. E. Poling, J. M. Prausnitz, and J. P. O'Connell, *The Properties of Gases and Liquids*. 2001.

[57] S. Saha and J. J. Carroll, "The isoenergetic-isochoric flash," *Fluid Phase Equilib.*, vol. 138, pp. 23–41, 1997.

[58] F. A. Aly and L. L. Lee, "Self-consistent equations for calculating the ideal gas heat capacity, enthalpy, and entropy," *Fluid Phase Equilib.*, vol. 6, no. 3–4, pp. 169–179, 1981.

[59] G. Wilczek-Vera and J. H. Vera, "Understanding cubic equations of state: A search for the hidden clues of their success," *AIChE J.*, vol. 61, no. 9, pp. 2824–2831, 2015.

[60] J. Bohbot, N. Gillet, and A. Benkenida, "IFP-C3D: an Unstructured Parallel Solver for Reactive Compressible Gas Flow with Spray," *Oil Gas Sci. Technol.*, vol. 64(3), no. 3, pp. 309–335, 2009.

[61] S. Patankar, *Numerical heat transfer and fluid flow: Computational methods in mechanics and thermal science*. 1980.

[62] A. Zein, M. Hantke, and G. Warnecke, "Modeling phase transition for compressible two-phase flows applied to metastable liquids," *J. Comput. Phys.*, vol. 229, no. 8, pp. 2964–2998, 2010.

[63] A. Chiapolino, P. Boivin, and R. Saurel, "A simple and fast phase transition relaxation solver for compressible multicomponent two-phase flows," *Comput. Fluids*, vol. 150, pp. 31–45, 2017.

[64] B. Li, Y. Gu, and M. Chen, "An experimental study on the cavitation of water with dissolved gases," *Exp. Fluids*, vol. 58, no. 12, pp. 1–9, 2017.

[65] P. J. Linstrom and W. G. Mallard, "The NIST Chemistry WebBook: A chemical data resource on the Internet," *J. Chem. Eng. Data*, vol. 46, no. 5, pp. 1059–1063, 2001.

[66] D. Duke *et al.*, "X-ray Imaging of Cavitation in Diesel Injectors," *SAE Int. J. Engines*, vol. 7, no. 2, pp. 2014-01–1404, 2014.

[67] D. J. Duke, "https://daniel-duke.net/media/ : Synchrotron X-ray Radiography of Nozzle Cavitation." .

[68] C. Mauger, L. Méès, M. Michard, A. Azouzi, and S. Valette, "Shadowgraph, Schlieren and interferometry in a 2D cavitating channel flow," *Exp. Fluids*, vol. 53, no. 6, pp. 1895–1913, 2012.

[69] S. Gopalan and J. Katz, "Flow structure and modeling issues in the closure region of attached cavitation," *Phys. Fluids*, vol. 12, no. 4, 2000.

[70] P. Yi, S. Jafari, S. Yang, and C. Habchi, "Numerical analysis of subcritical evaporation and transcritical mixing of droplet using a tabulated multicomponent vapor-liquid equilibrium model," in *ILASS–Europe 2019, 29th Conference on Liquid Atomization and Spray Systems*, 2019.

[71] S. Brown *et al.*, "Thermodynamic interpolation for the simulation of two-phase flow of non-ideal mixtures," *Comput. Chem. Eng.*, vol. 95, pp. 49–57, 2006.

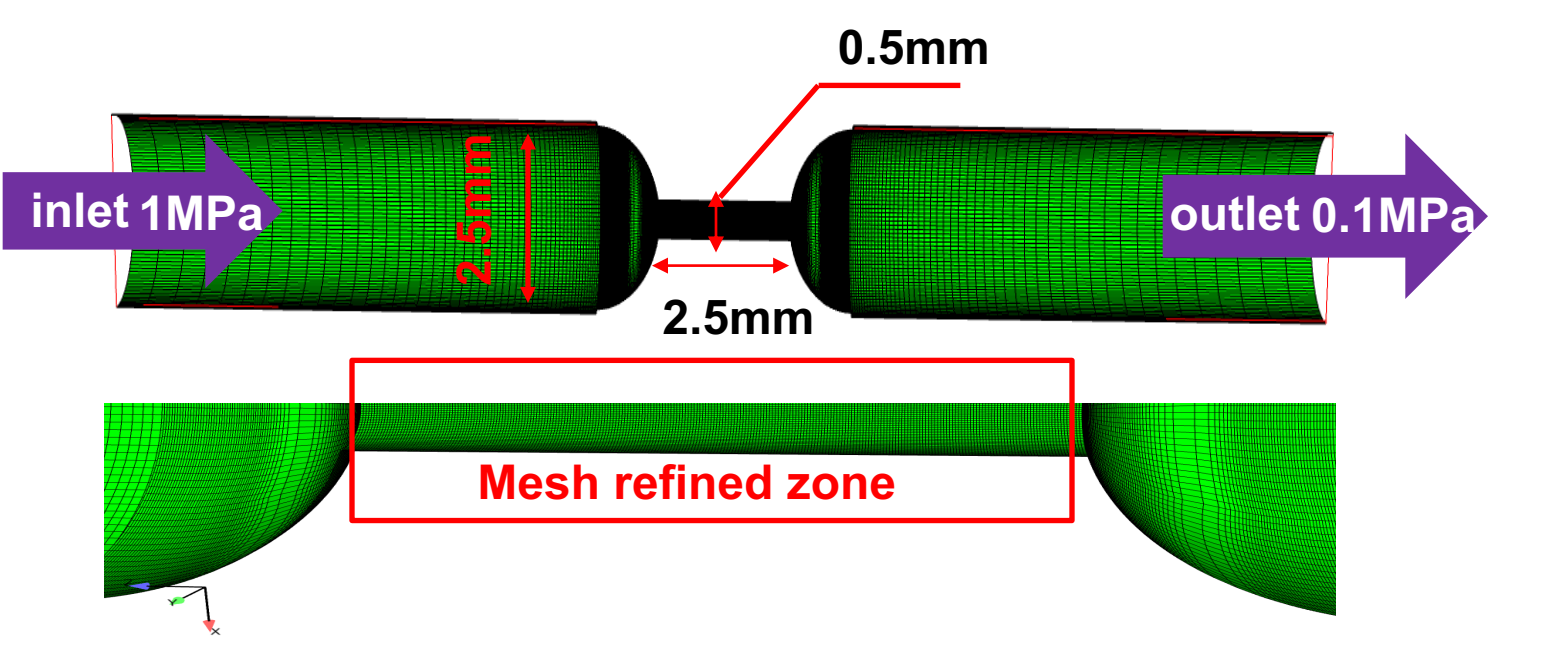
0.5mm
inlet 1MPa
2.5mm
outlet 0.1MPa
2.5mm
Mesh refined zone

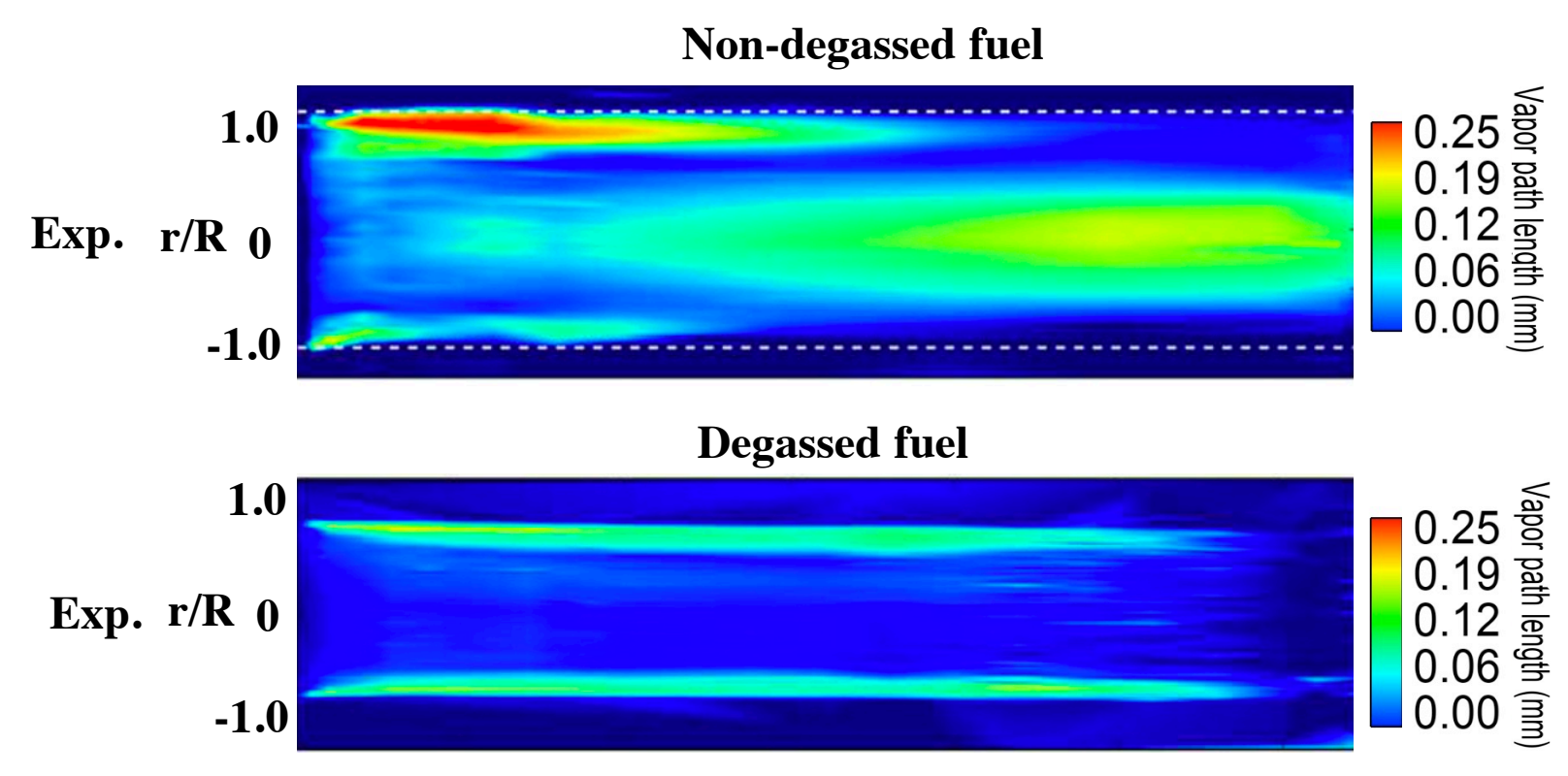
Non-degassed fuel
1.0
Exp. r/R 0
-1.0
0.25
0.19
0.12
0.06
0.00
Vapor path length (mm)
Degassed fuel
1.0
Exp. r/R 0
-1.0
0.25
0.19
0.12
0.06
0.00
Vapor path length (mm)

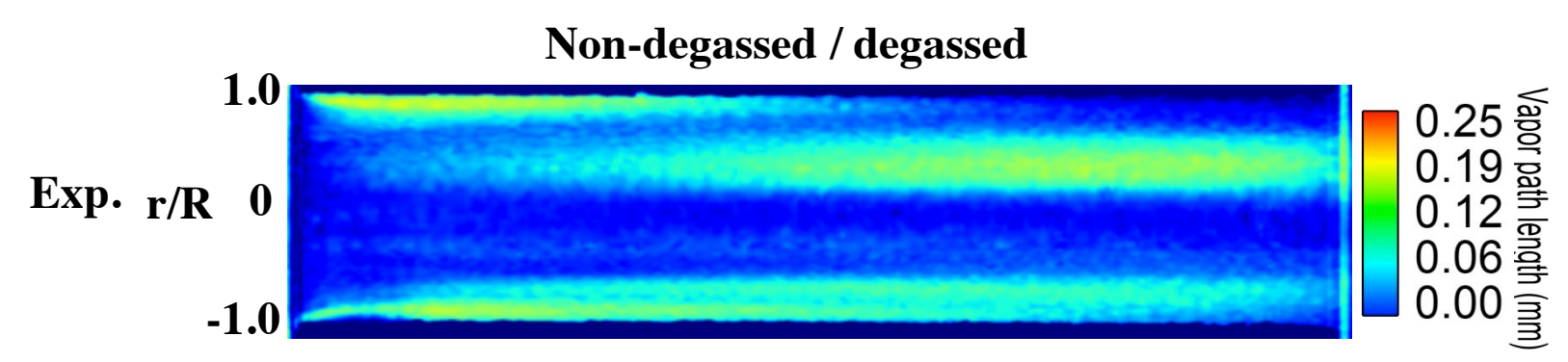
Non-degassed / degassed
1.0
Exp.
r/R
0
-1.0
0.25
0.19
0.12
0.06
0.00
Vapor path length (mm)

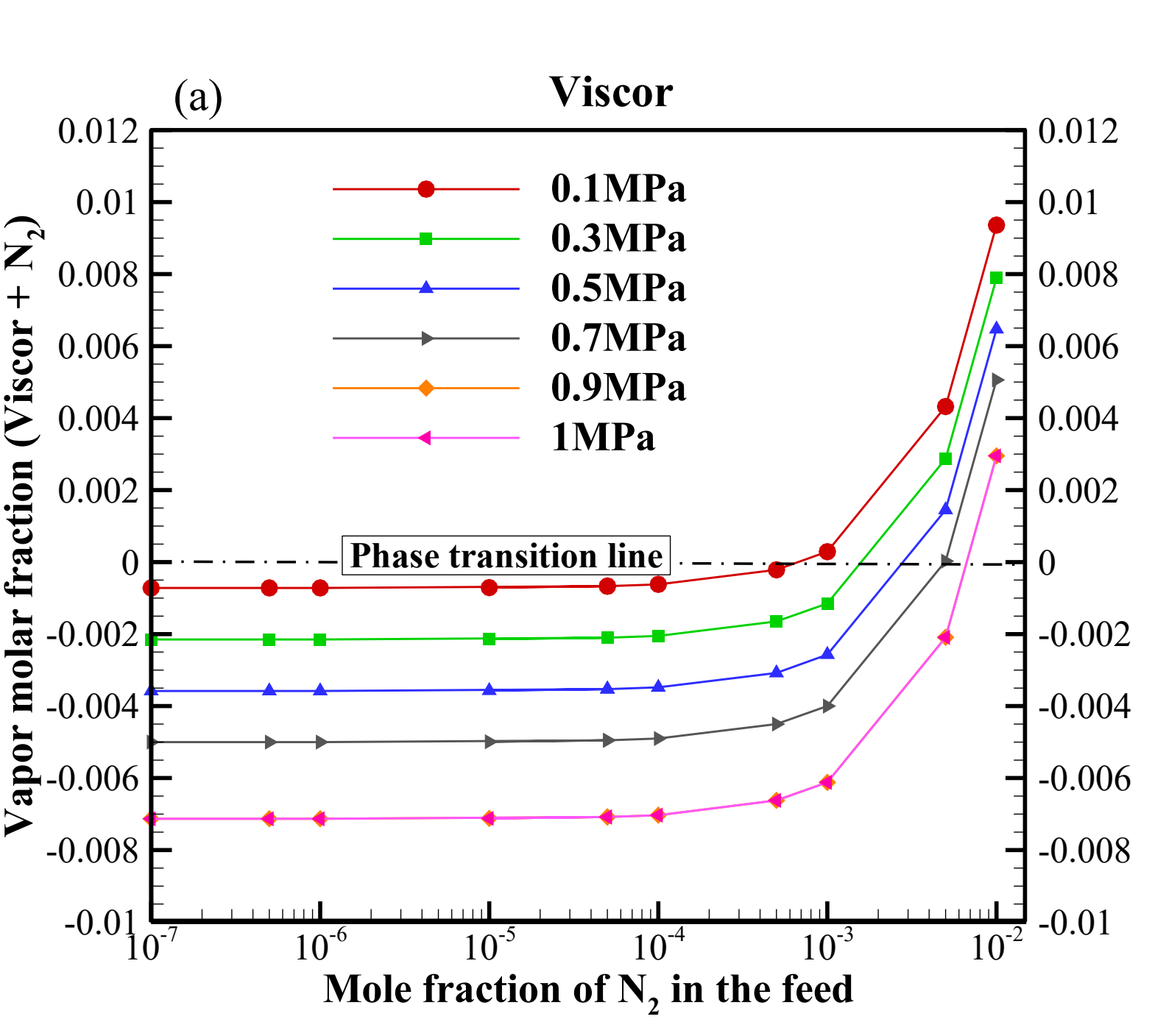
(a)
Viscor
0.1MPa
0.3MPa
0.5MPa
0.7MPa
0.9MPa
1MPa
Phase transition line
Vapor molar fraction (Viscor + N2)
Mole fraction of N2 in the feed
0.012
0.01
0.008
0.006
0.004
0.002
0
-0.002
-0.004
-0.006
-0.008
-0.01
10-7
10-6
10-5
10-4
10-3
10-2

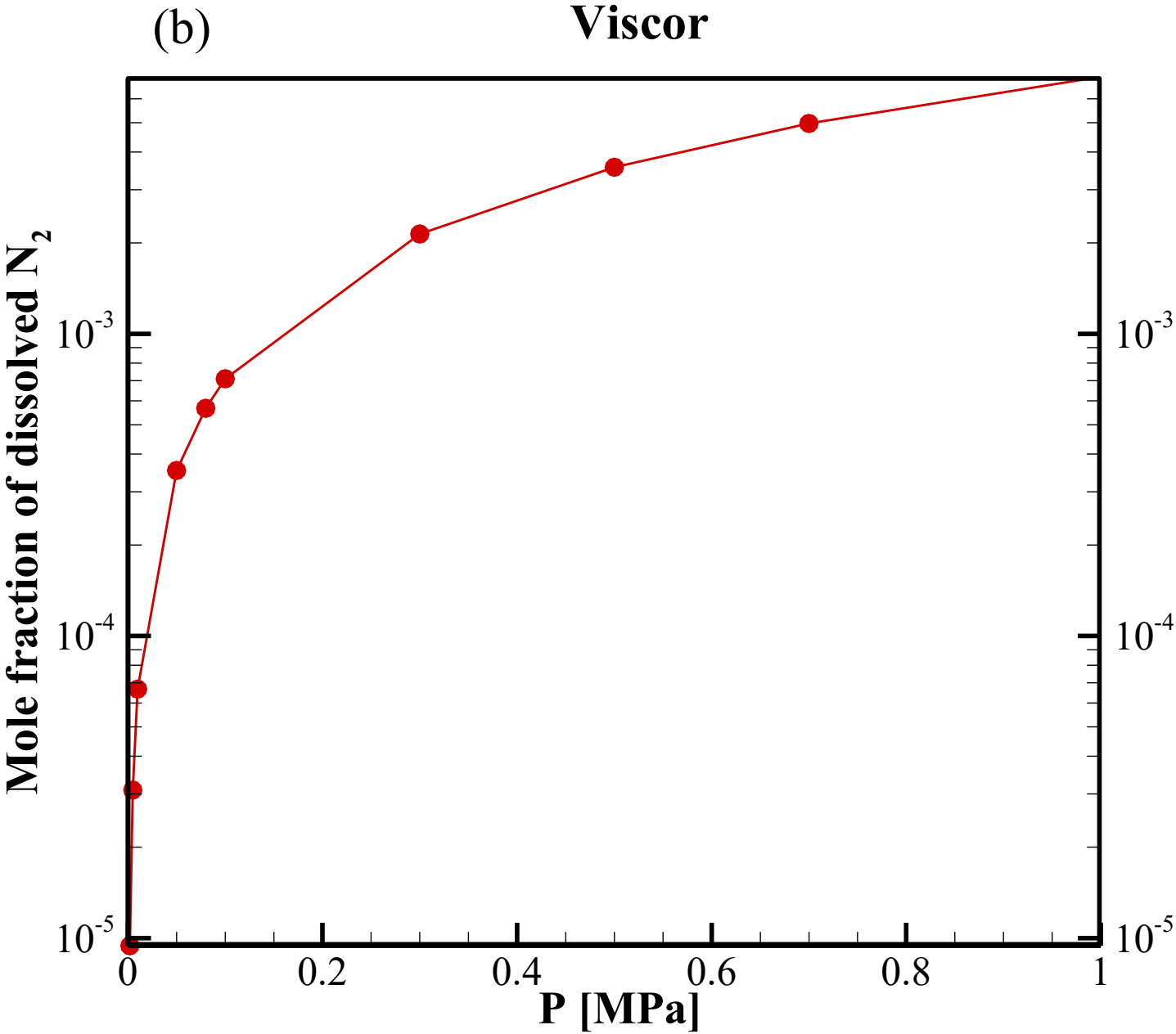
(b)
Viscor
Mole fraction of dissolved N_2
10^{-3}
10^{-4}
10^{-5}
0
0.2
0.4
0.6
0.8
1
P [MPa]

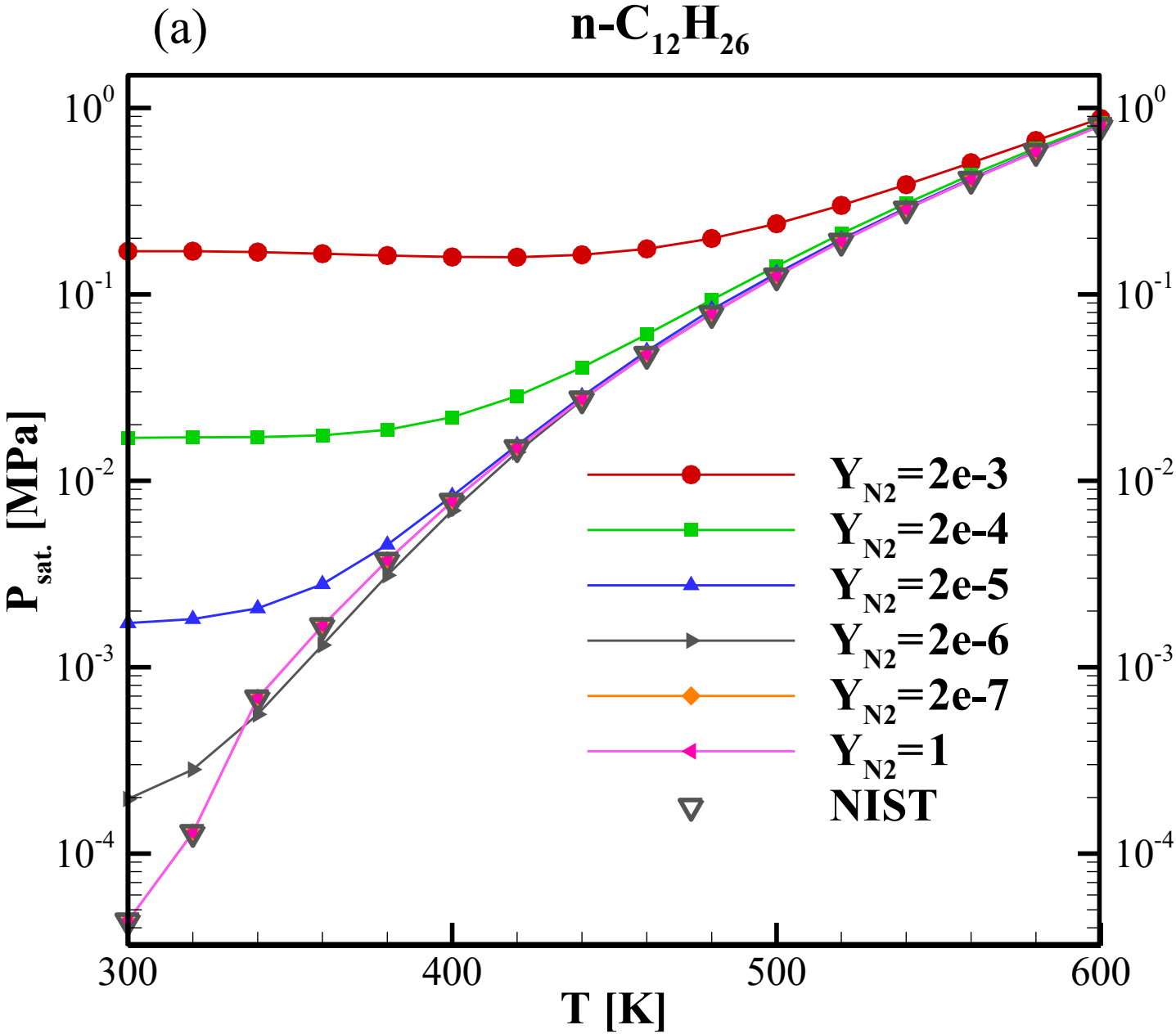
(a)
n-C12H26
P sat. [MPa]
T [K]
10^0
10^-1
10^-2
10^-3
10^-4
300
400
500
600
Y N2=2e-3
Y N2=2e-4
Y N2=2e-5
Y N2=2e-6
Y N2=2e-7
Y N2=1
NIST

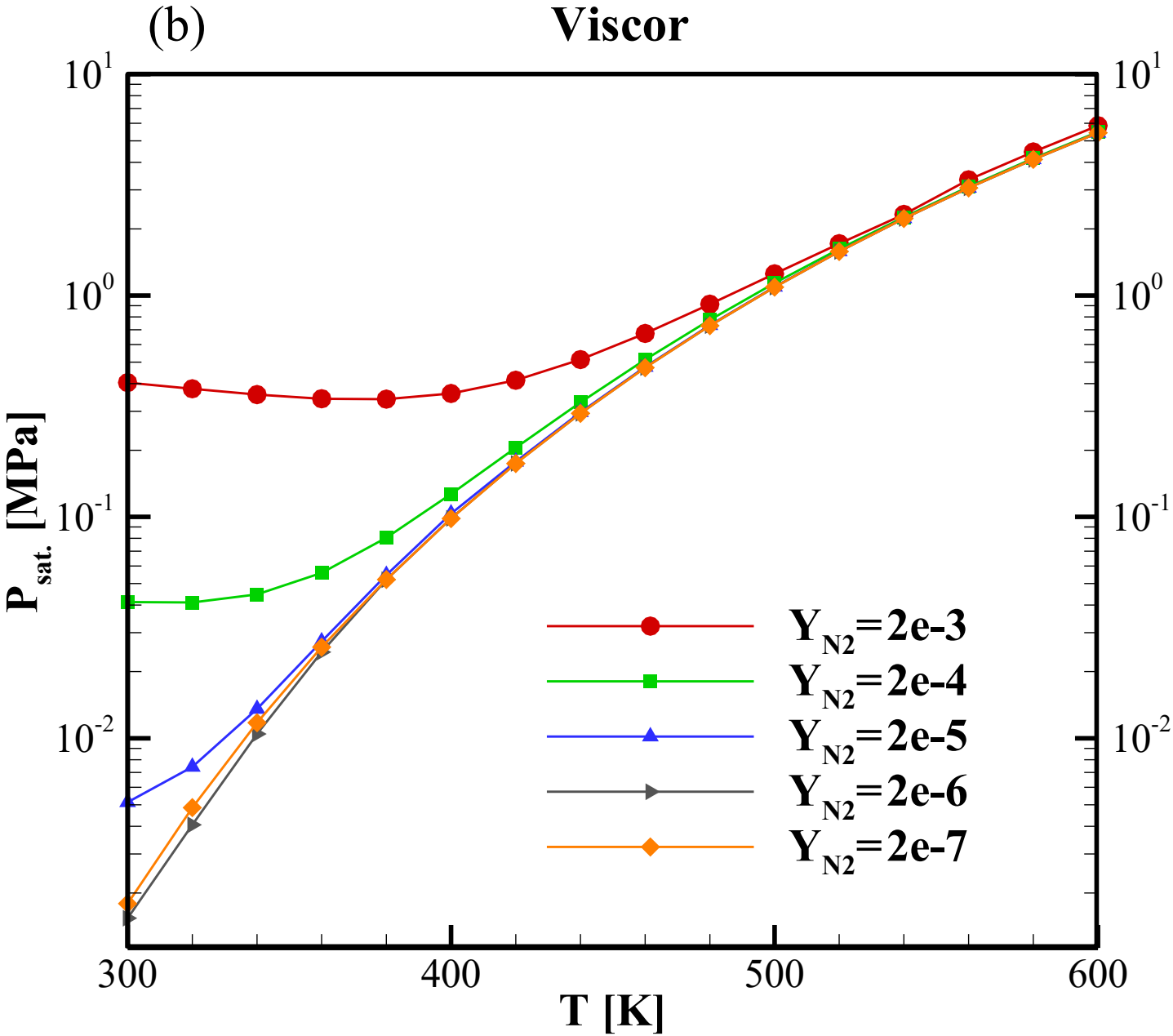
(b)
Viscor
10^1
10^0
10^{-1}
10^{-2}
$P_{sat.}$ [MPa]
300
400
500
600
T [K]
Y_{N2}=2e-3
Y_{N2}=2e-4
Y_{N2}=2e-5
Y_{N2}=2e-6
Y_{N2}=2e-7

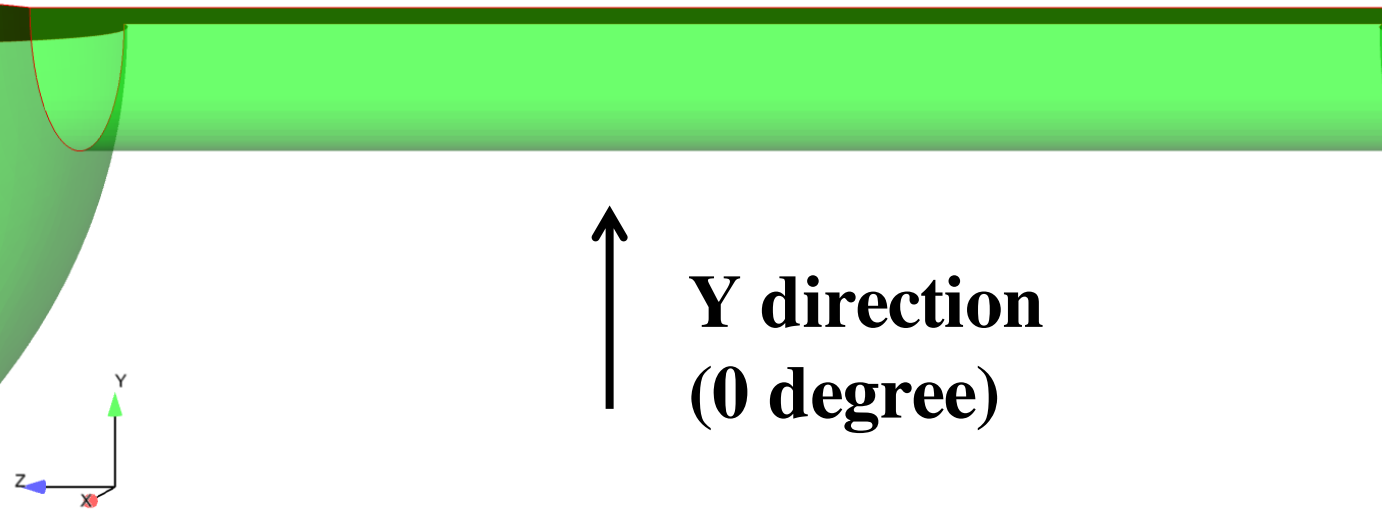
Y direction
(0 degree)
Y
Z
X

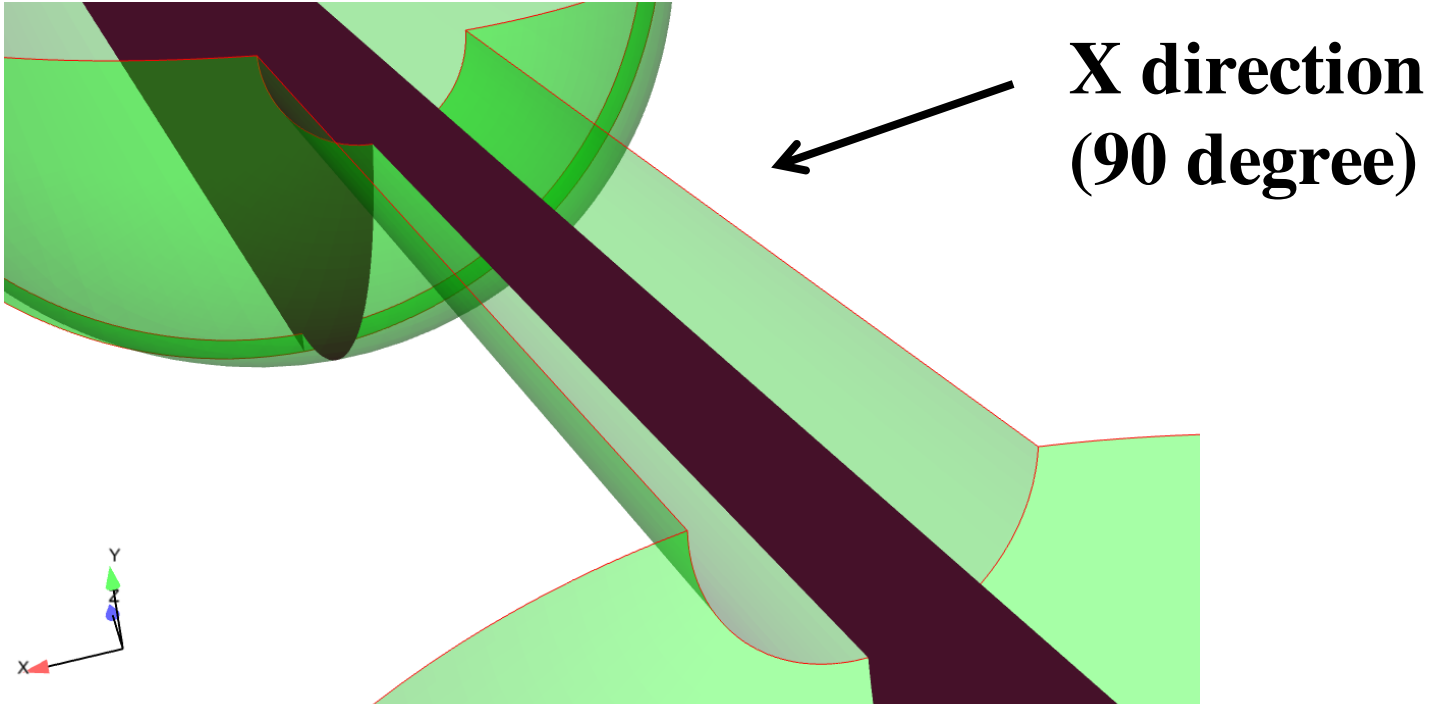
X direction
(90 degree)
Y
X

Exp.
(Non-degas)

Exp.
(Degas)

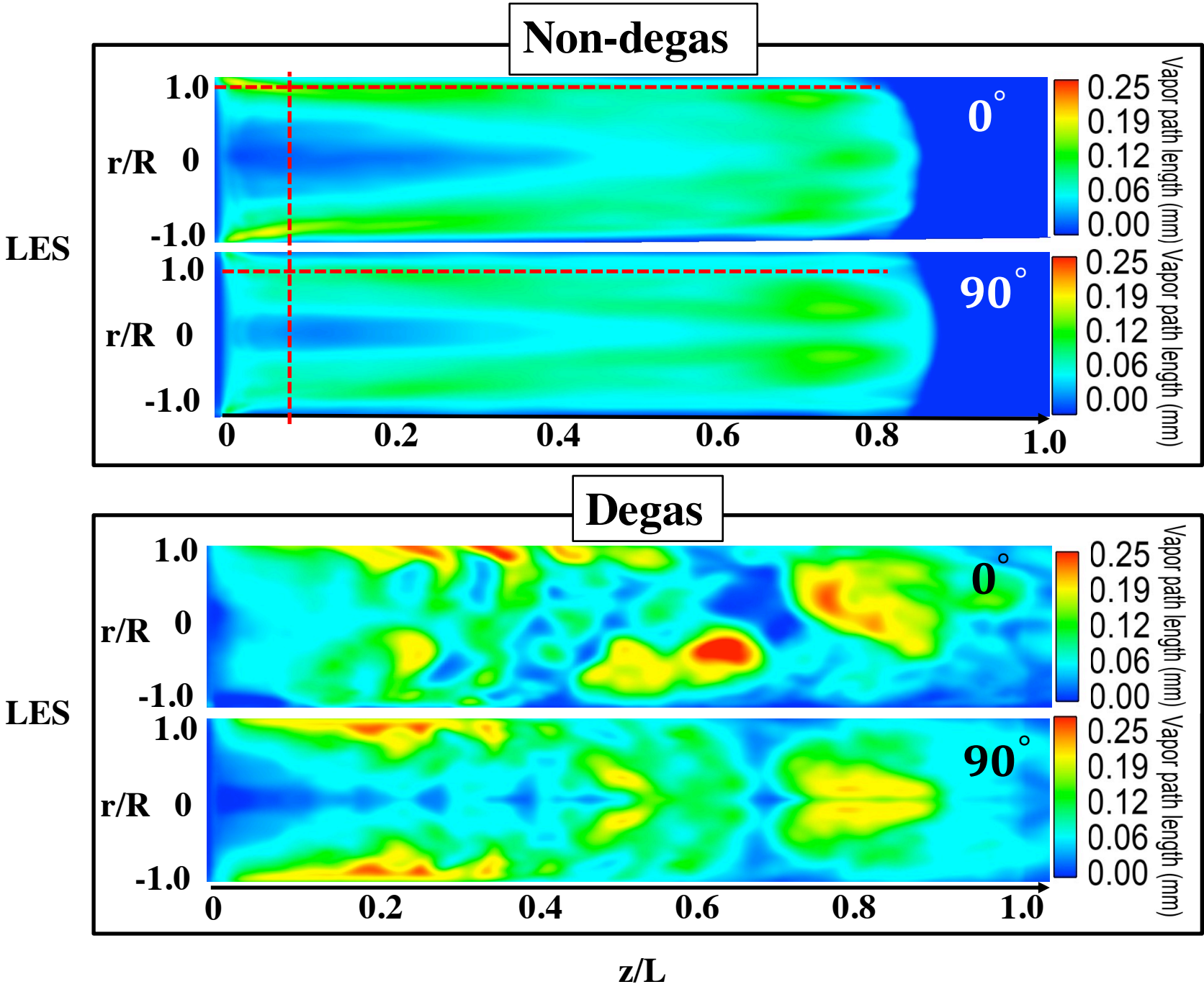
Non-degas
LES
1.0
r/R 0
-1.0
0°
90°
0
0.2
0.4
0.6
0.8
1.0
Vapor path length (mm)
0.25
0.19
0.12
0.06
0.00
Degas
LES
z/L

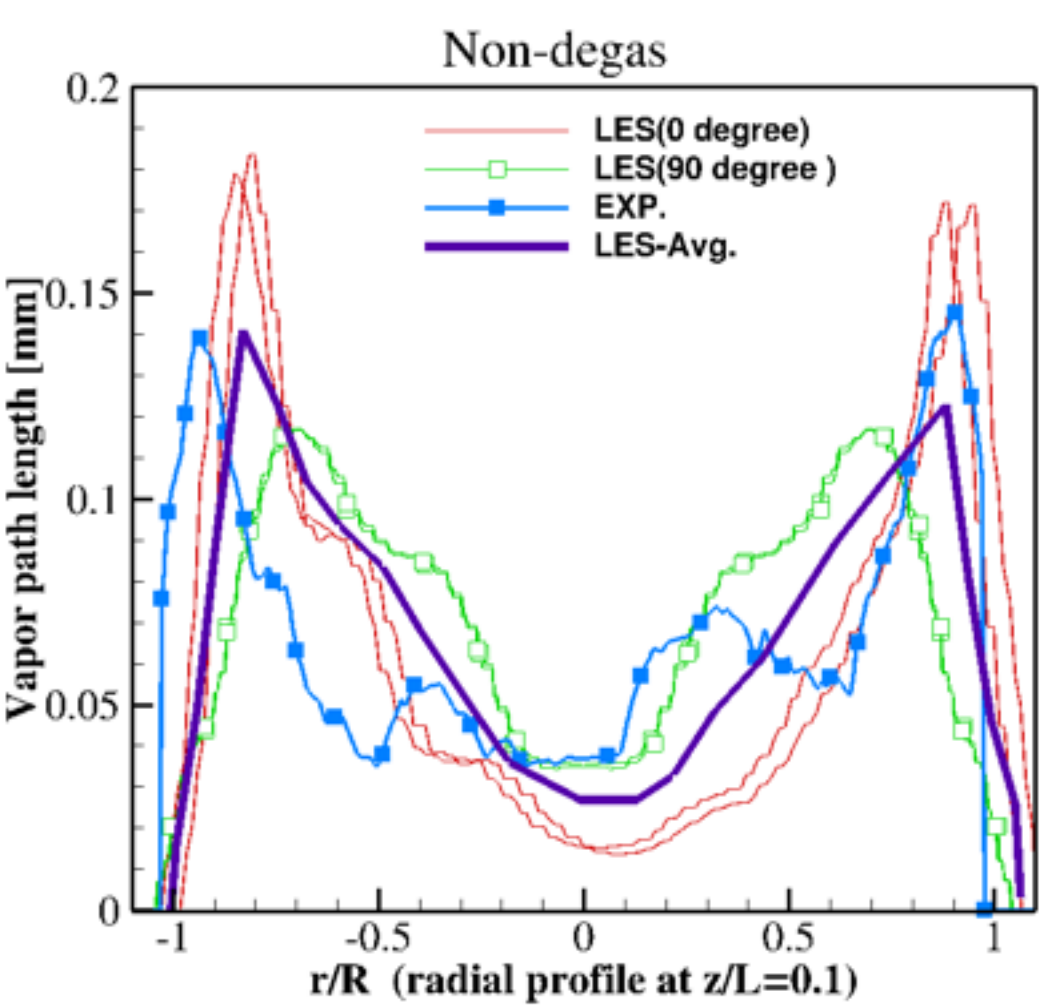
Non-degas
LES(0 degree)
LES(90 degree)
EXP.
LES-Avg.
Vapor path length [mm]
0.2
0.15
0.1
0.05
0
-1
-0.5
0
0.5
1
r/R (radial profile at z/L=0.1)

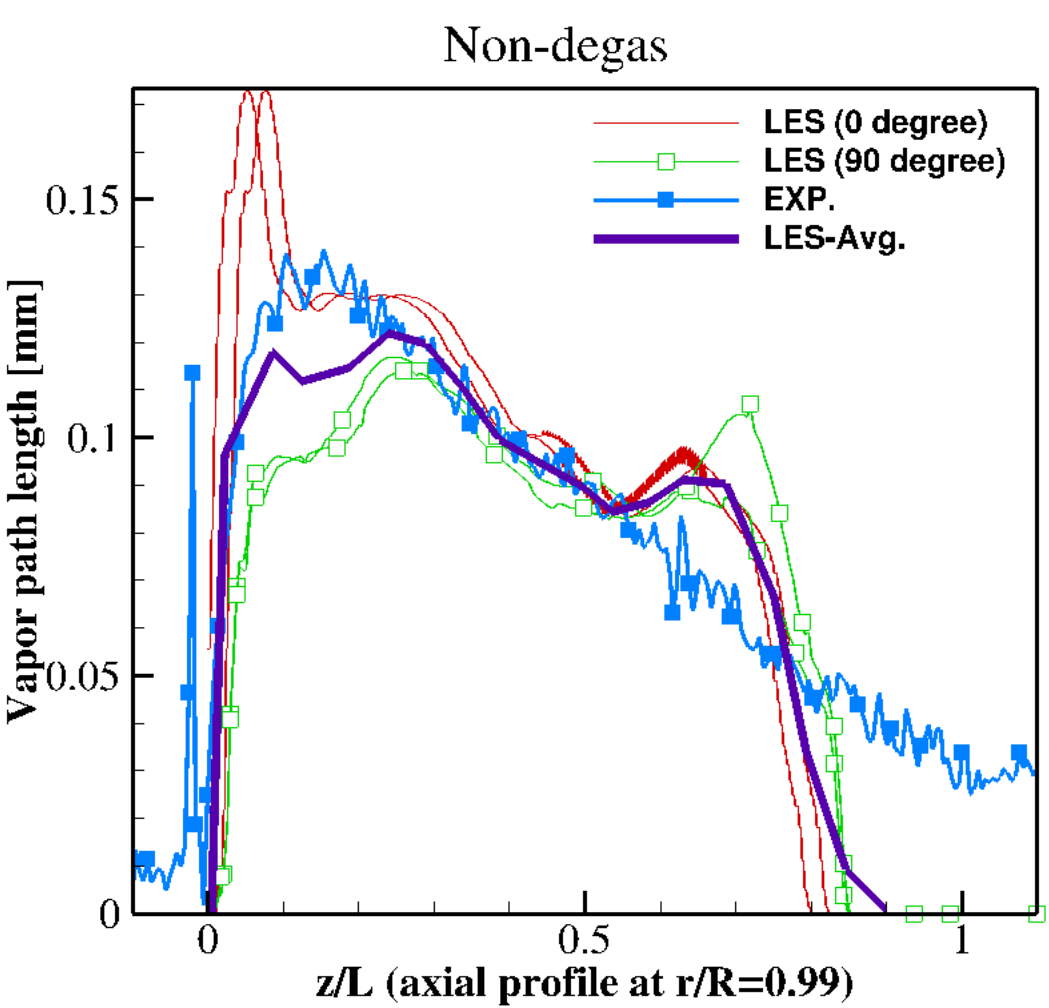
Non-degas
LES (0 degree)
LES (90 degree)
EXP.
LES-Avg.
Vapor path length [mm]
0.15
0.1
0.05
0
0
0.5
1
z/L (axial profile at r/R=0.99)

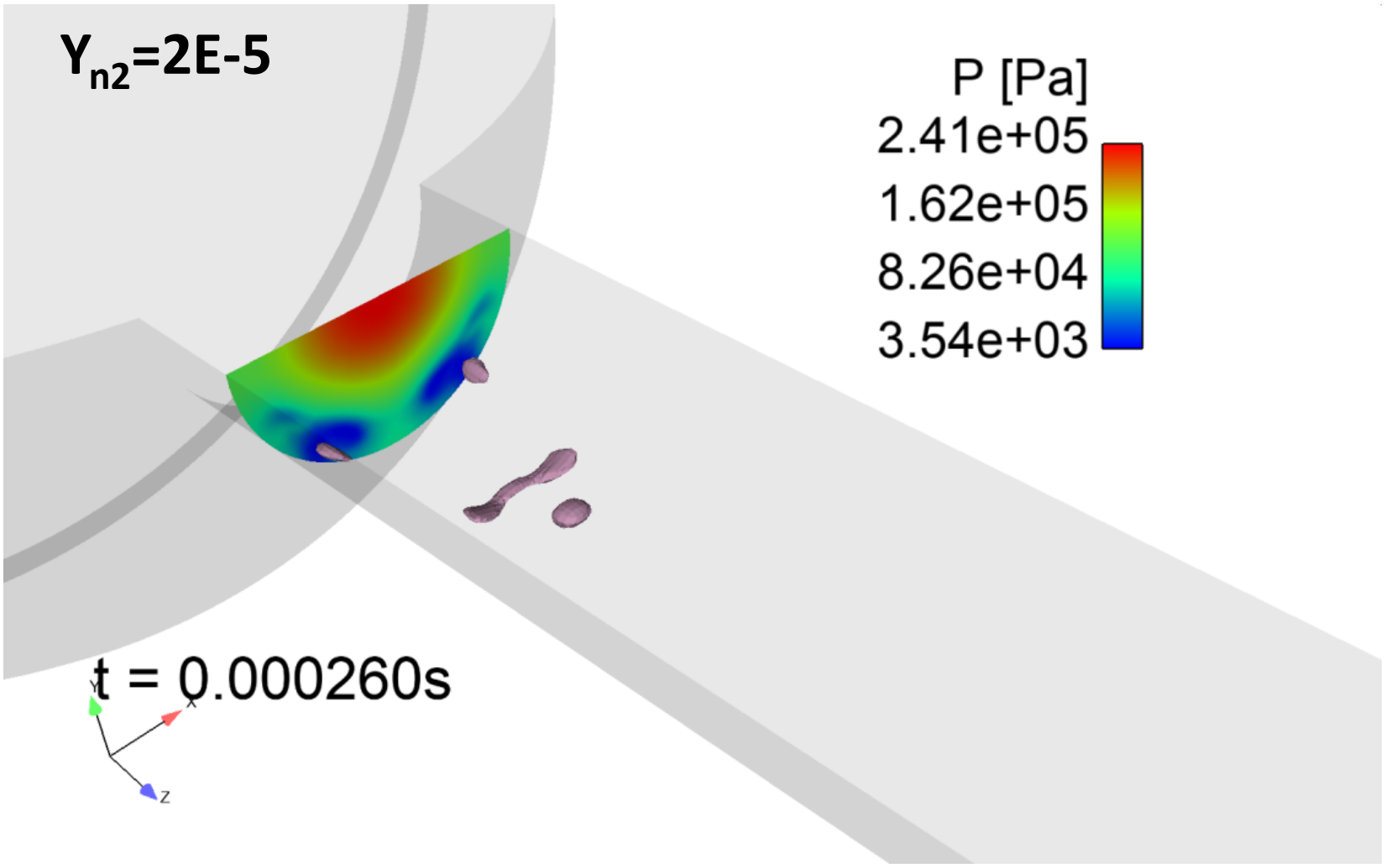
Y_{n2}=2E-5
P [Pa]
2.41e+05
1.62e+05
8.26e+04
3.54e+03
t = 0.000260s
Y
X
Z

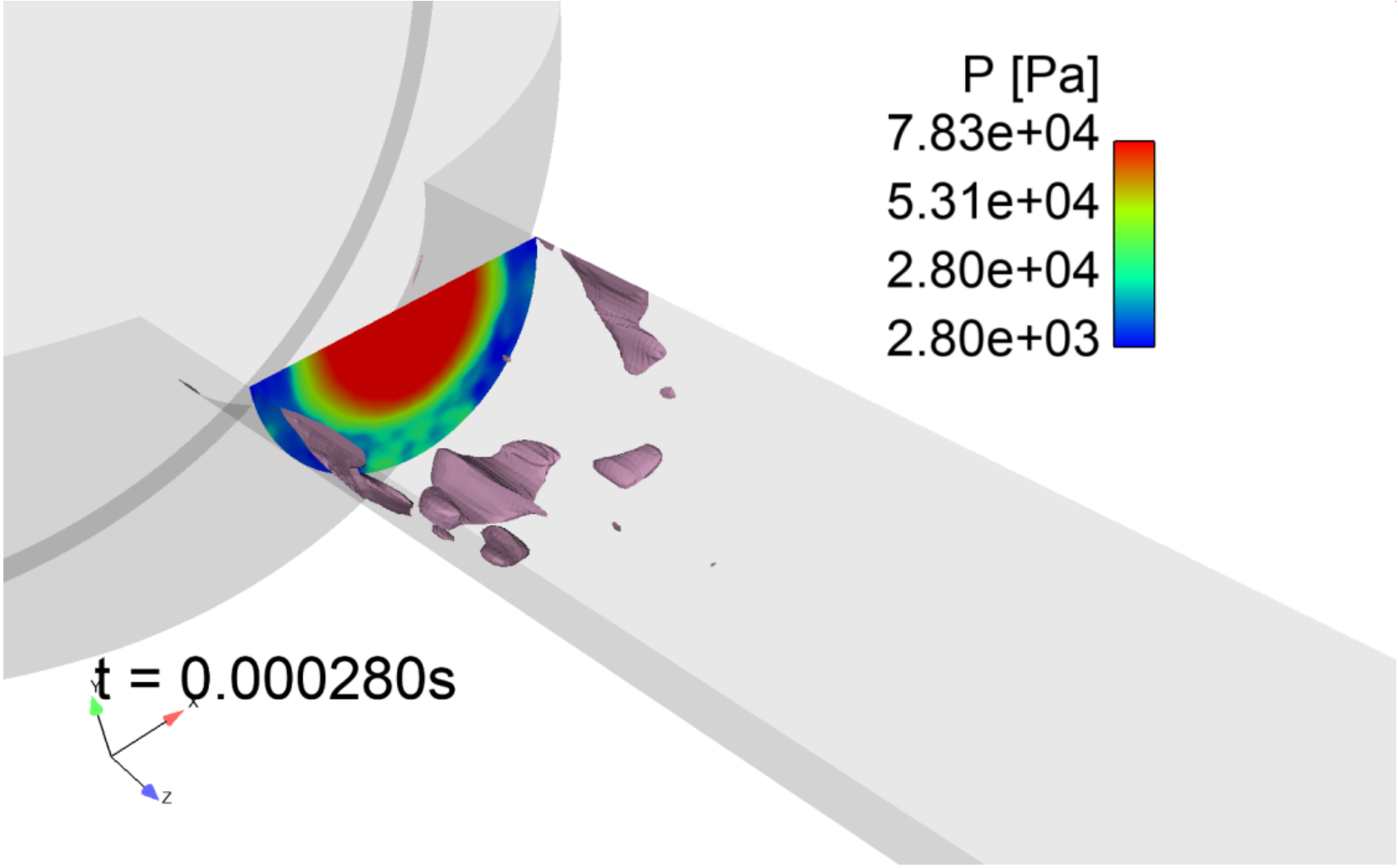
P [Pa]
7.83e+04
5.31e+04
2.80e+04
2.80e+03
t = 0.000280s
Y
X
Z

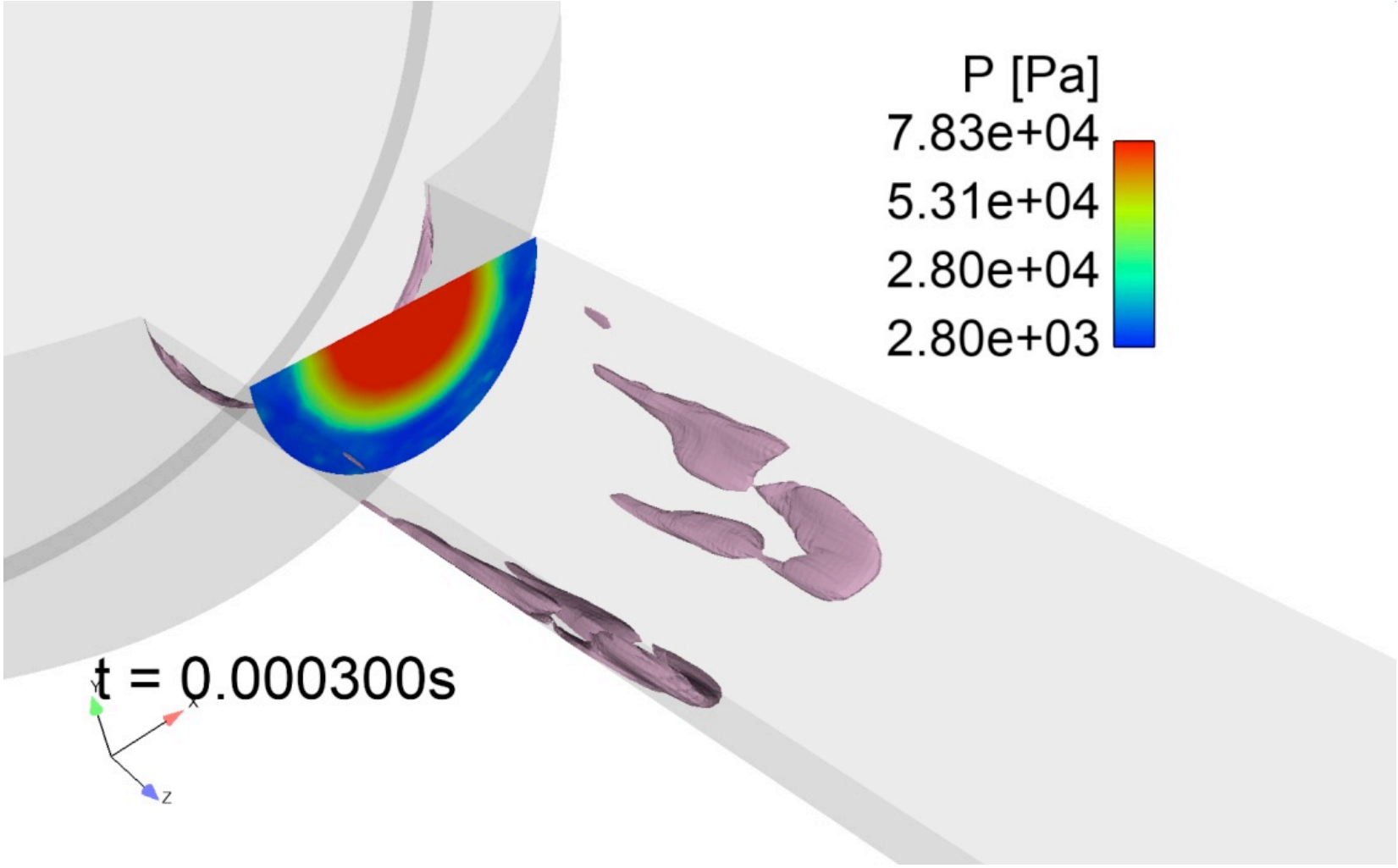
P [Pa]
7.83e+04
5.31e+04
2.80e+04
2.80e+03
t = 0.000300s
Y
X
Z

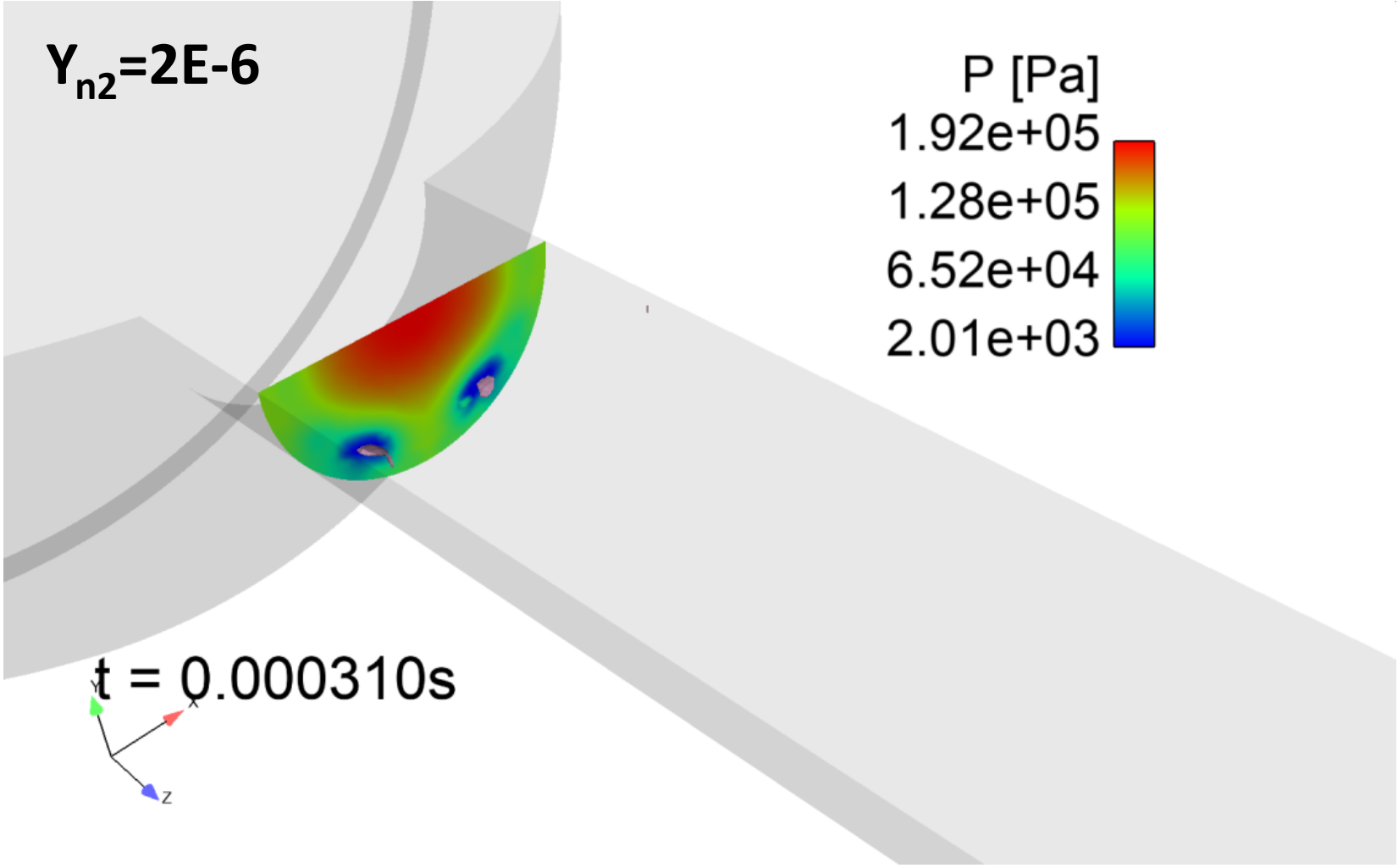
Y_{n2}=2E-6
P [Pa]
1.92e+05
1.28e+05
6.52e+04
2.01e+03
t = 0.000310s
Y
X
Z

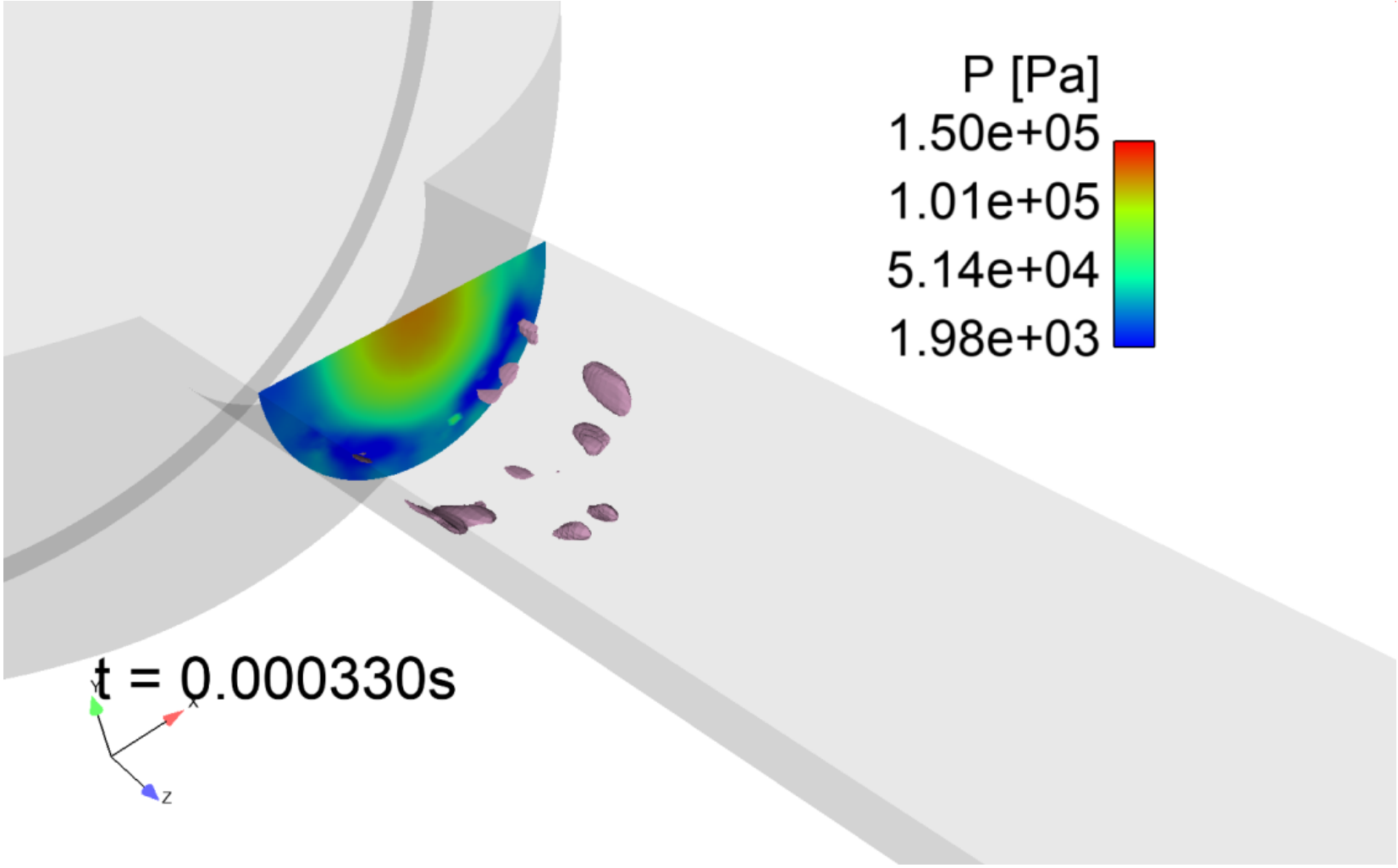
P [Pa]
1.50e+05
1.01e+05
5.14e+04
1.98e+03
t = 0.000330s
Y
X
Z

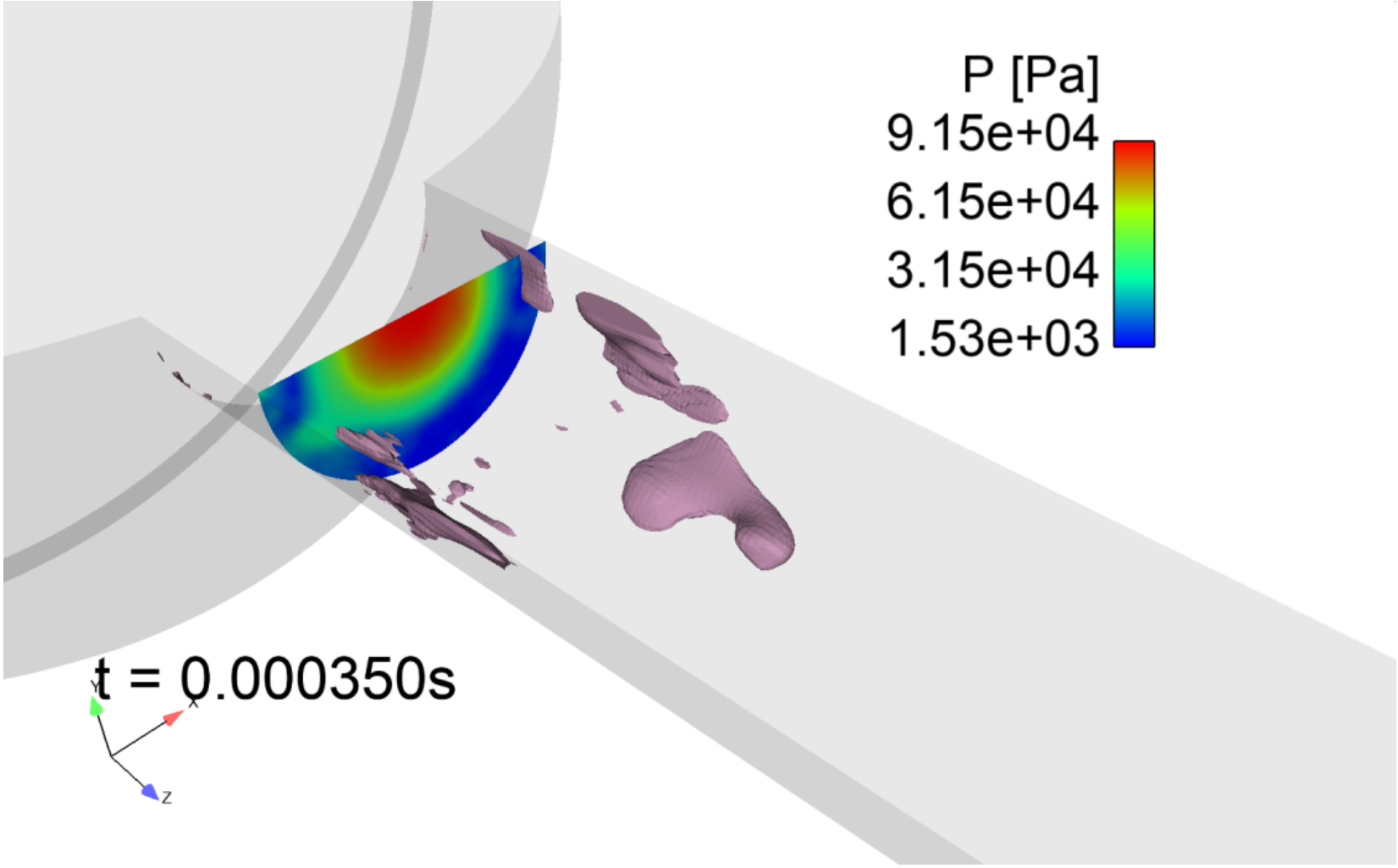
P [Pa]
9.15e+04
6.15e+04
3.15e+04
1.53e+03
t = 0.000350s
Y
X
Z

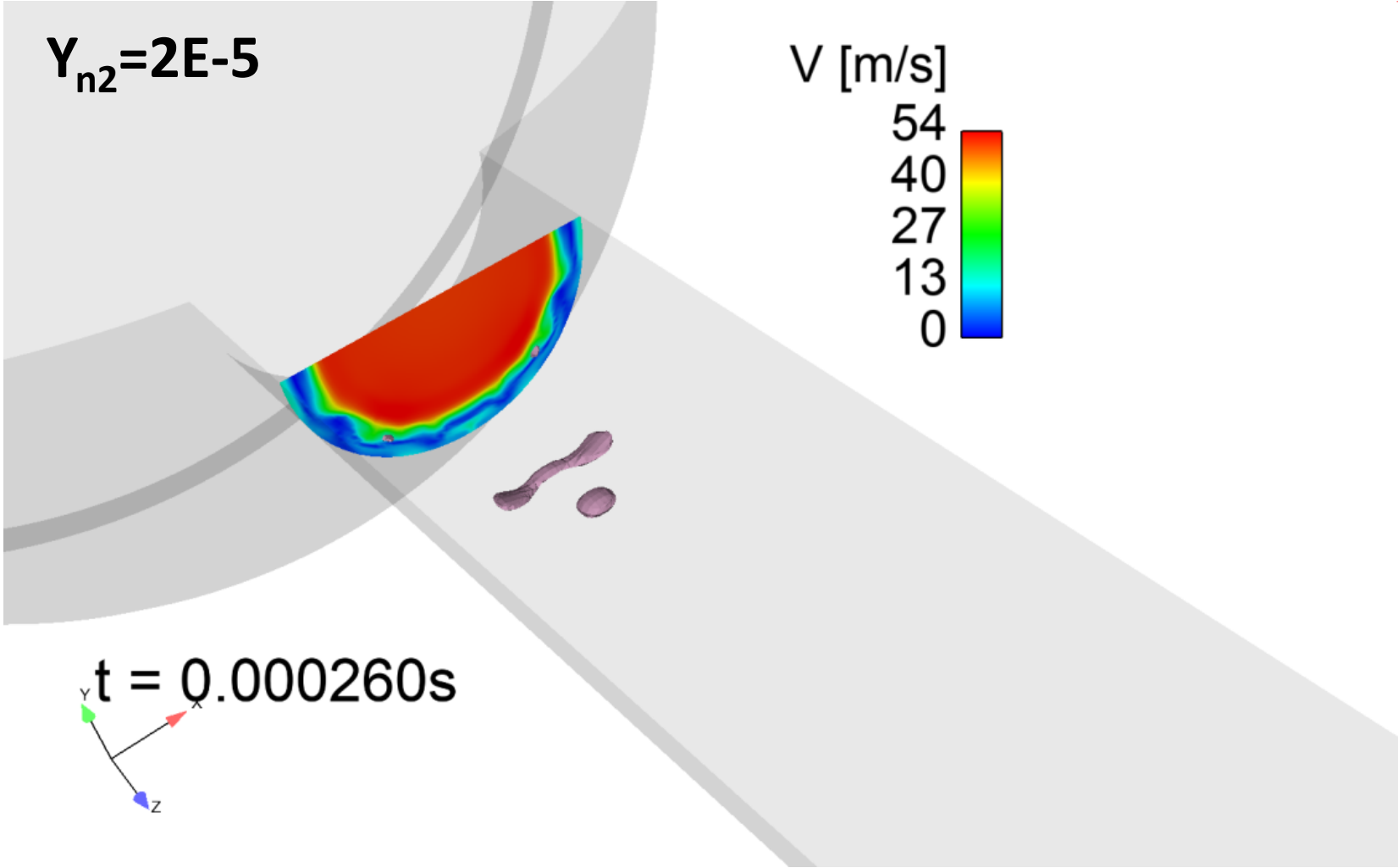
Y_{n2}=2E-5
V [m/s]
54
40
27
13
0
t = 0.000260s
Y
X
Z

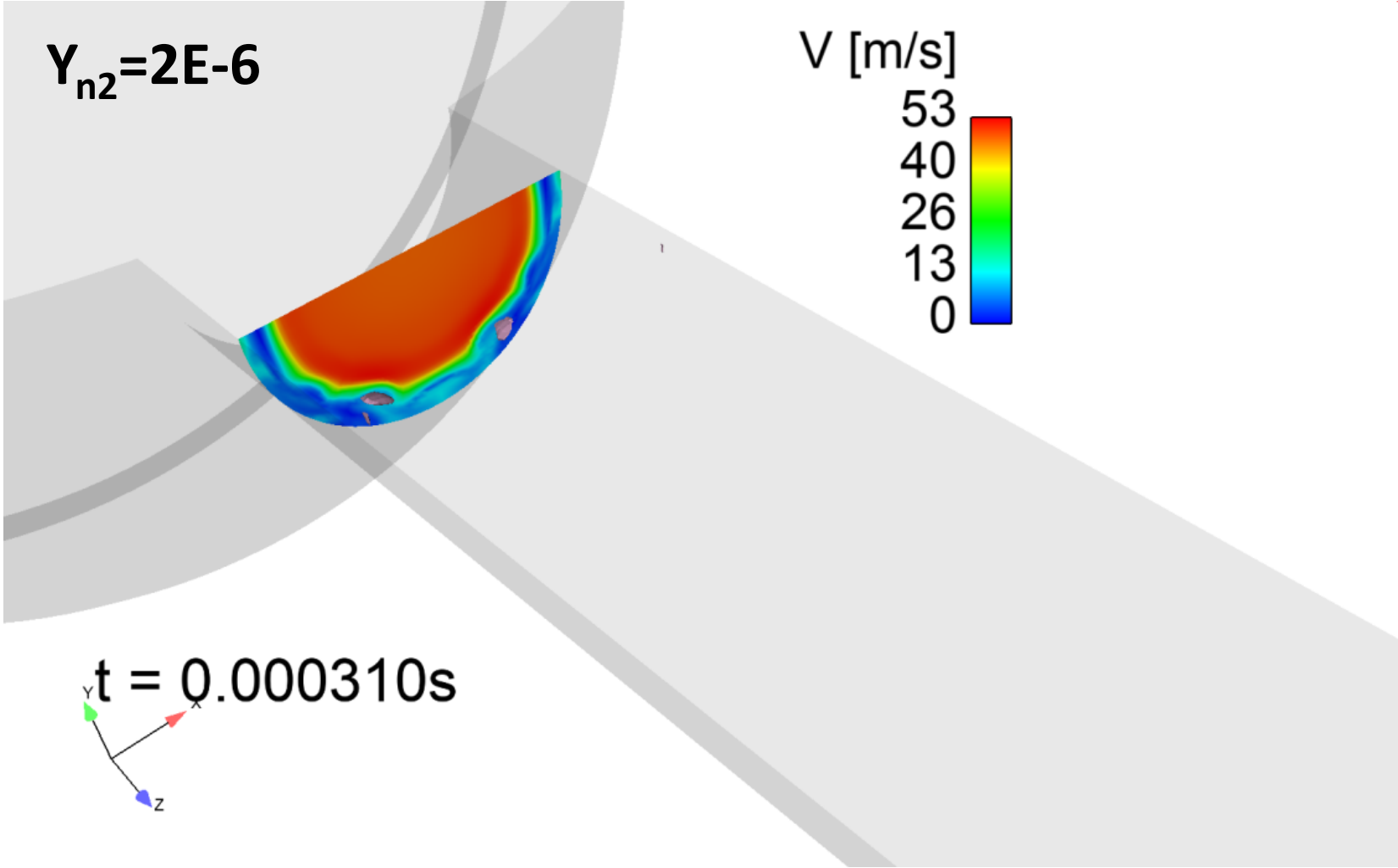
Y_{n2}=2E-6
V [m/s]
53
40
26
13
0
t = 0.000310s
Y
X
Z

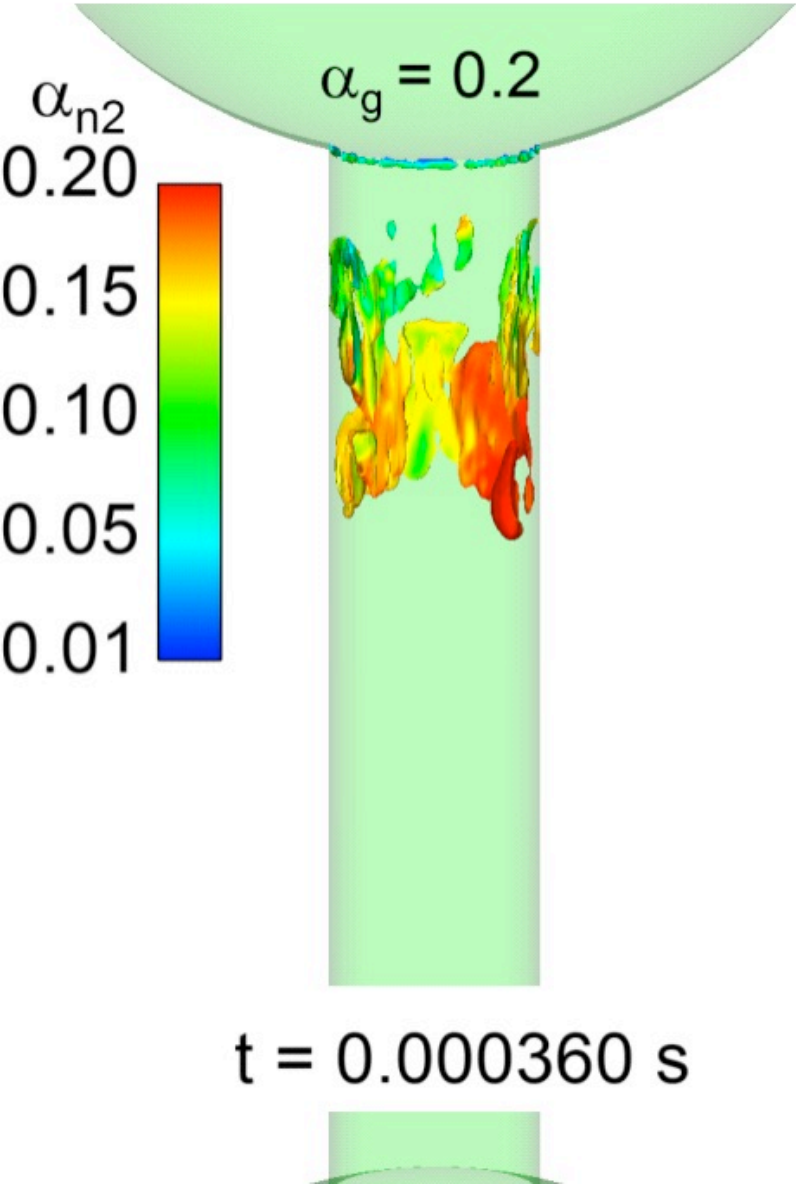
$\alpha_g = 0.2$
α_{n2}
0.20
0.15
0.10
0.05
0.01
t = 0.000360 s

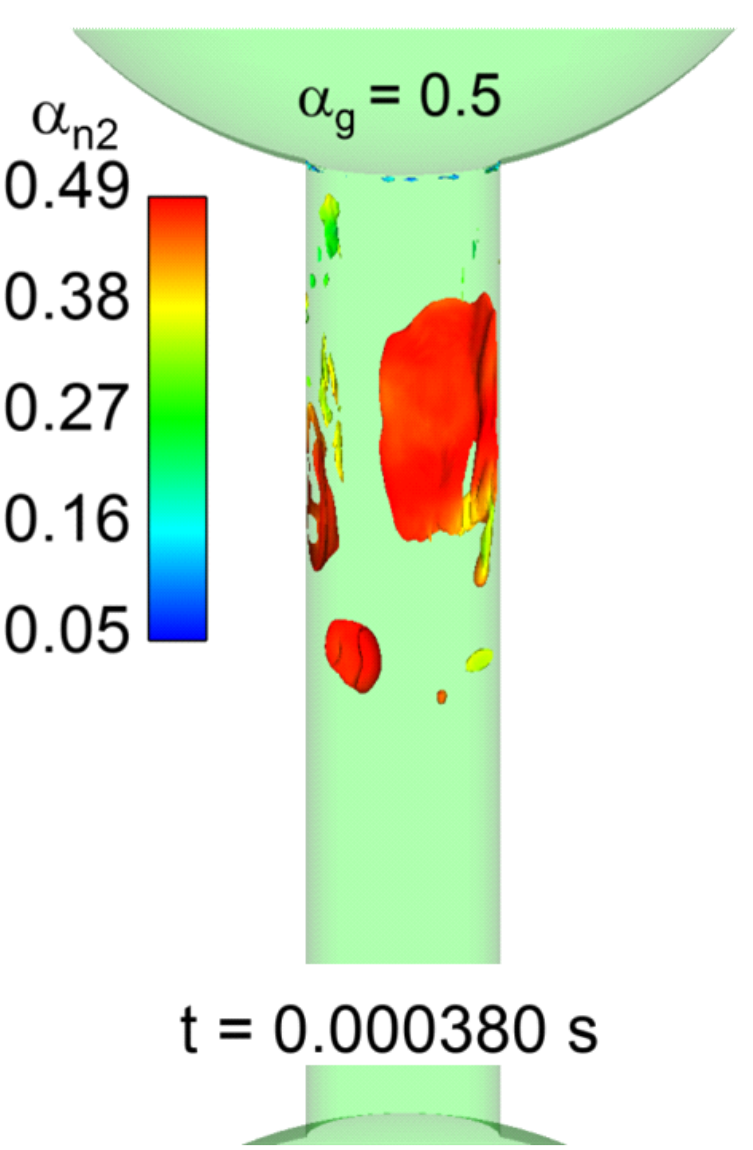
α_{n2}
0.49
0.38
0.27
0.16
0.05
$\alpha_g = 0.5$
t = 0.000380 s

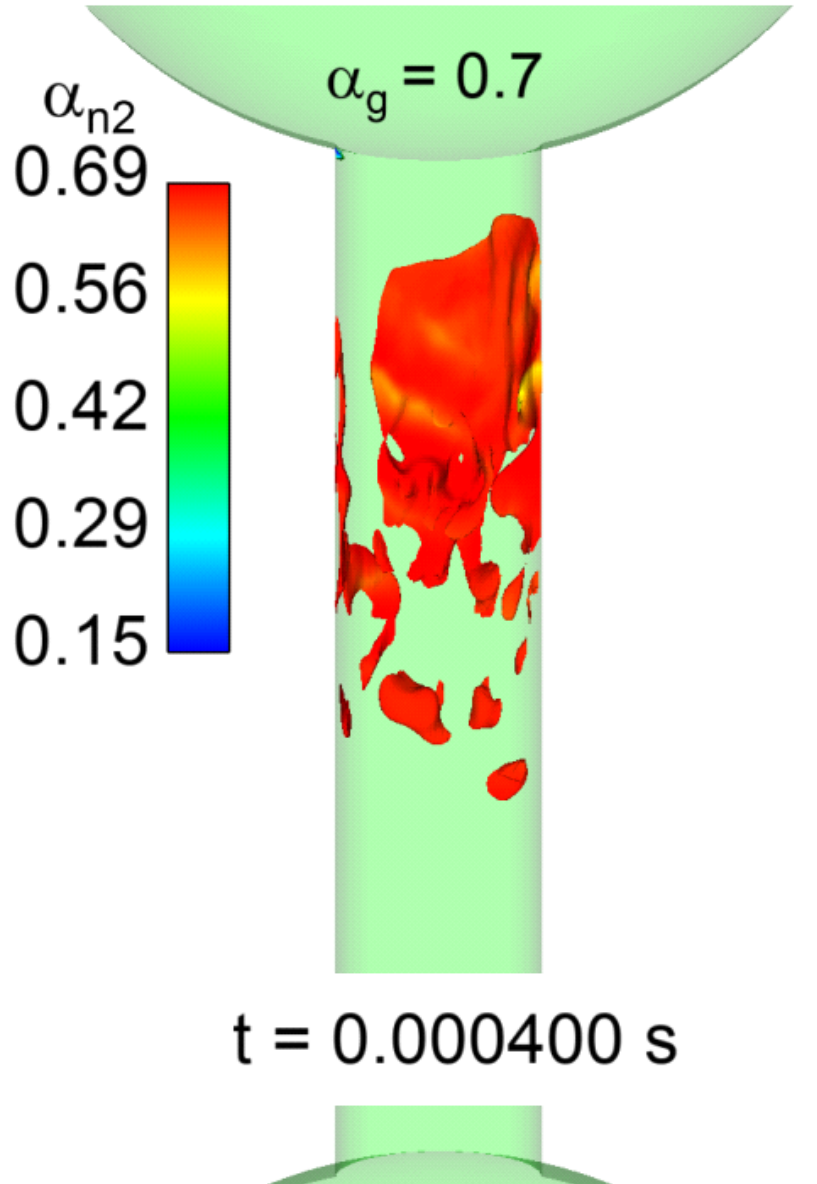
α_{n2}
0.69
0.56
0.42
0.29
0.15
$\alpha_g = 0.7$
t = 0.000400 s

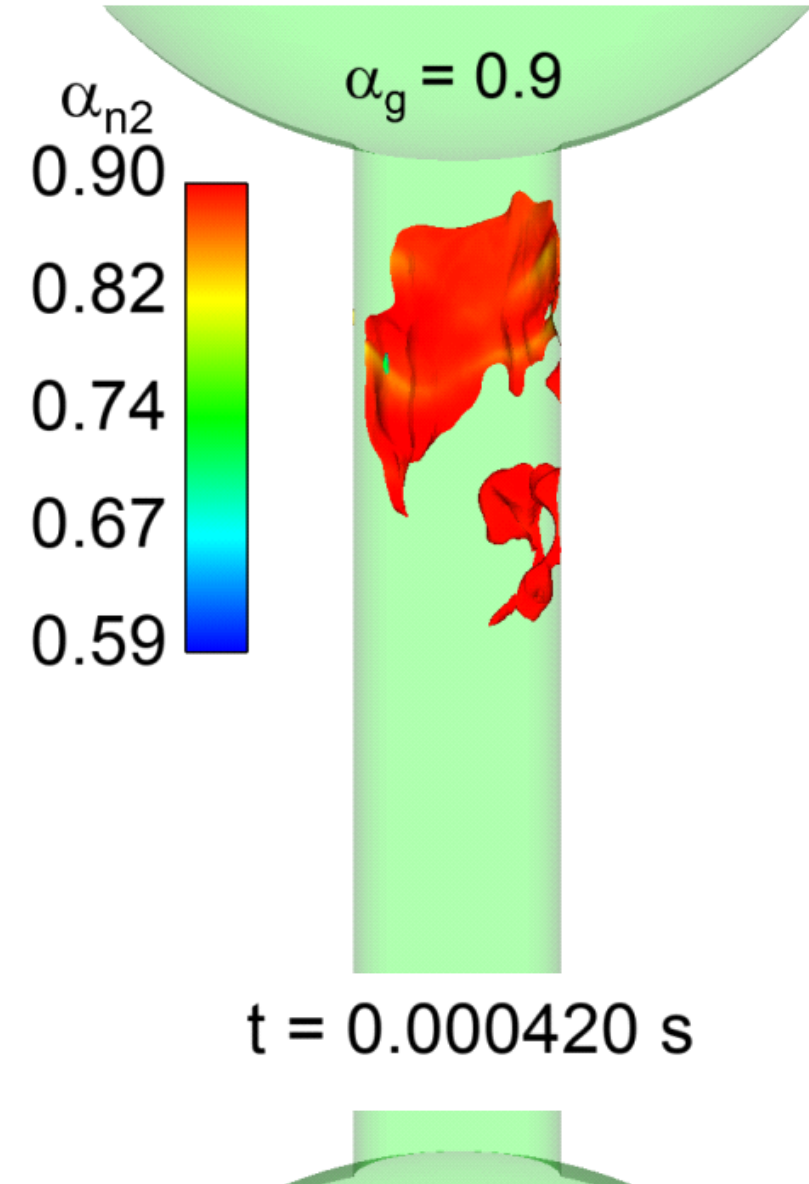
α_{n2}
0.90
0.82
0.74
0.67
0.59
$\alpha_g = 0.9$
t = 0.000420 s

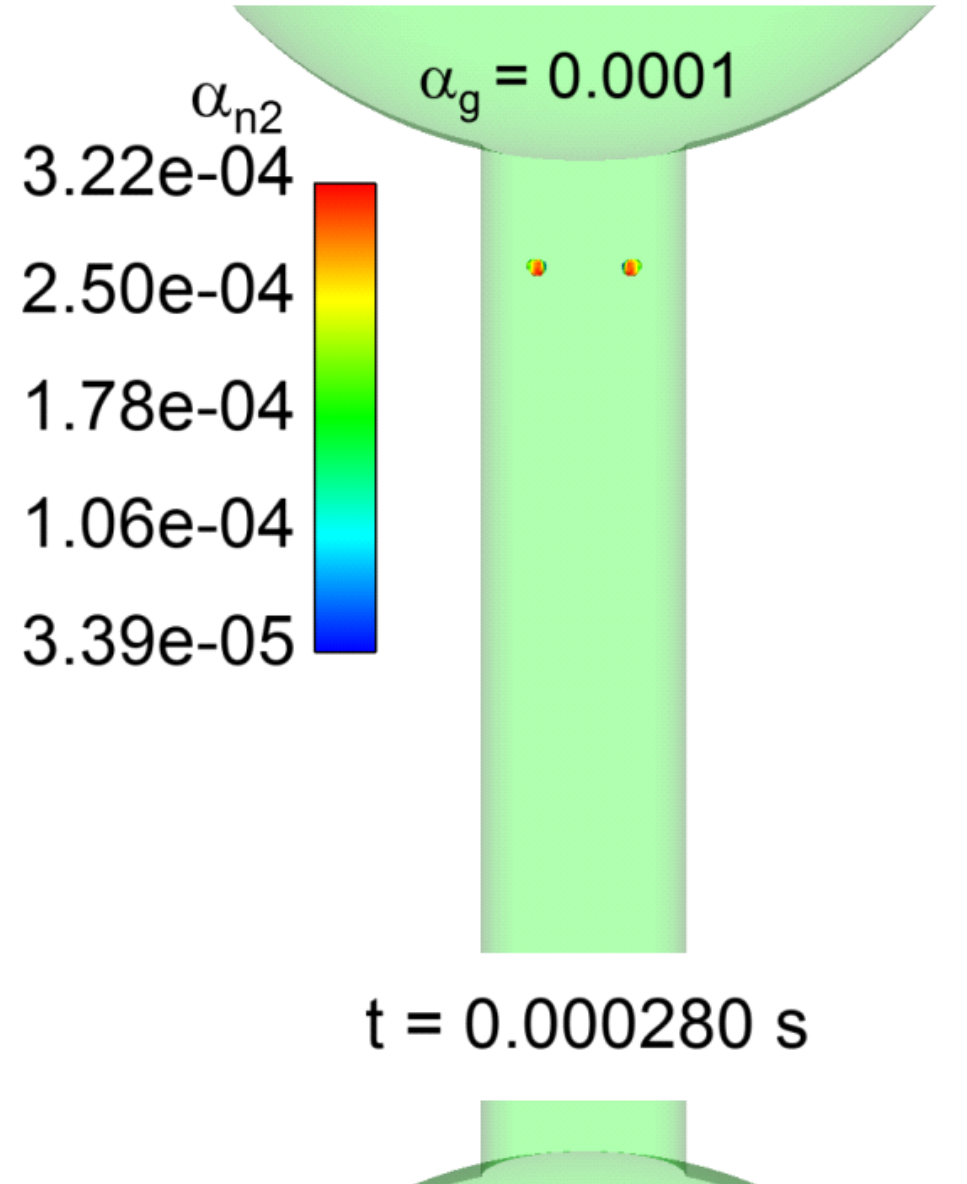
α_g = 0.0001
α_{n2}
3.22e-04
2.50e-04
1.78e-04
1.06e-04
3.39e-05
t = 0.000280 s

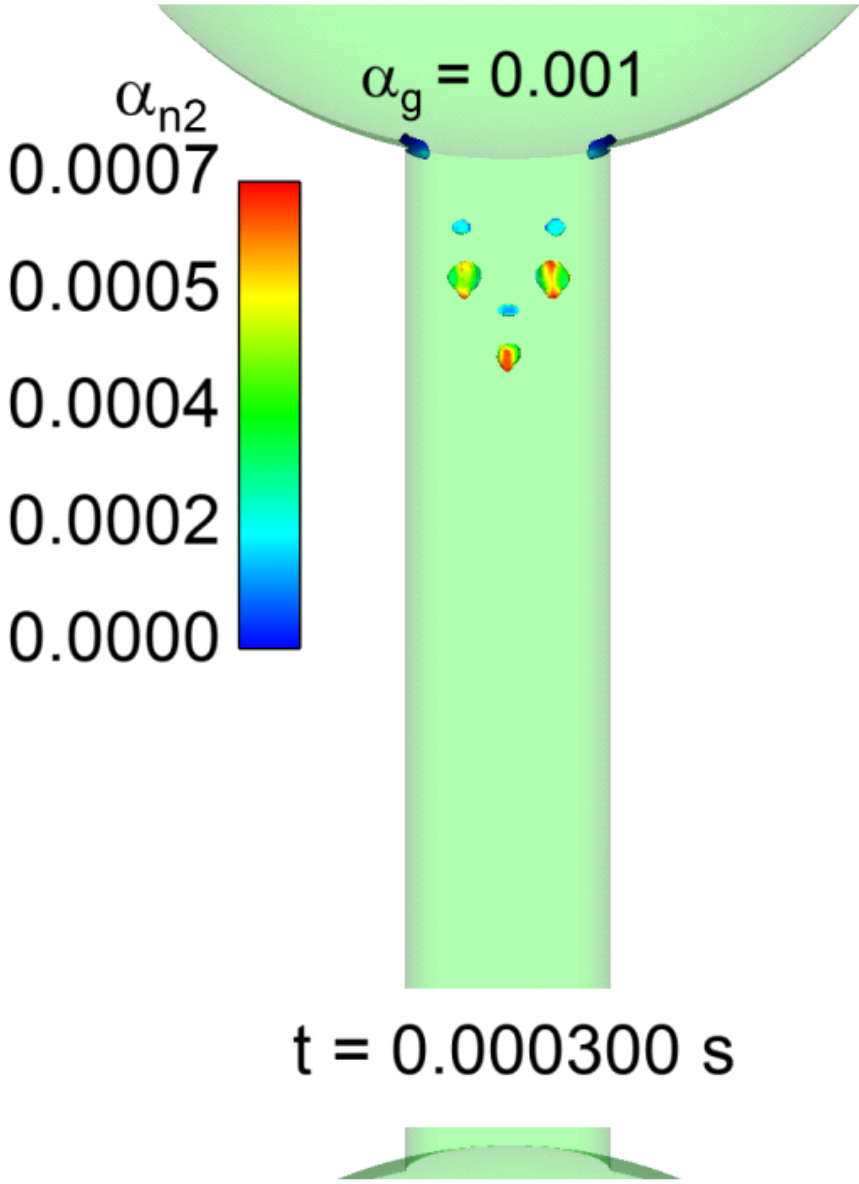
α_g = 0.001
α_{n2}
0.0007
0.0005
0.0004
0.0002
0.0000
t = 0.000300 s

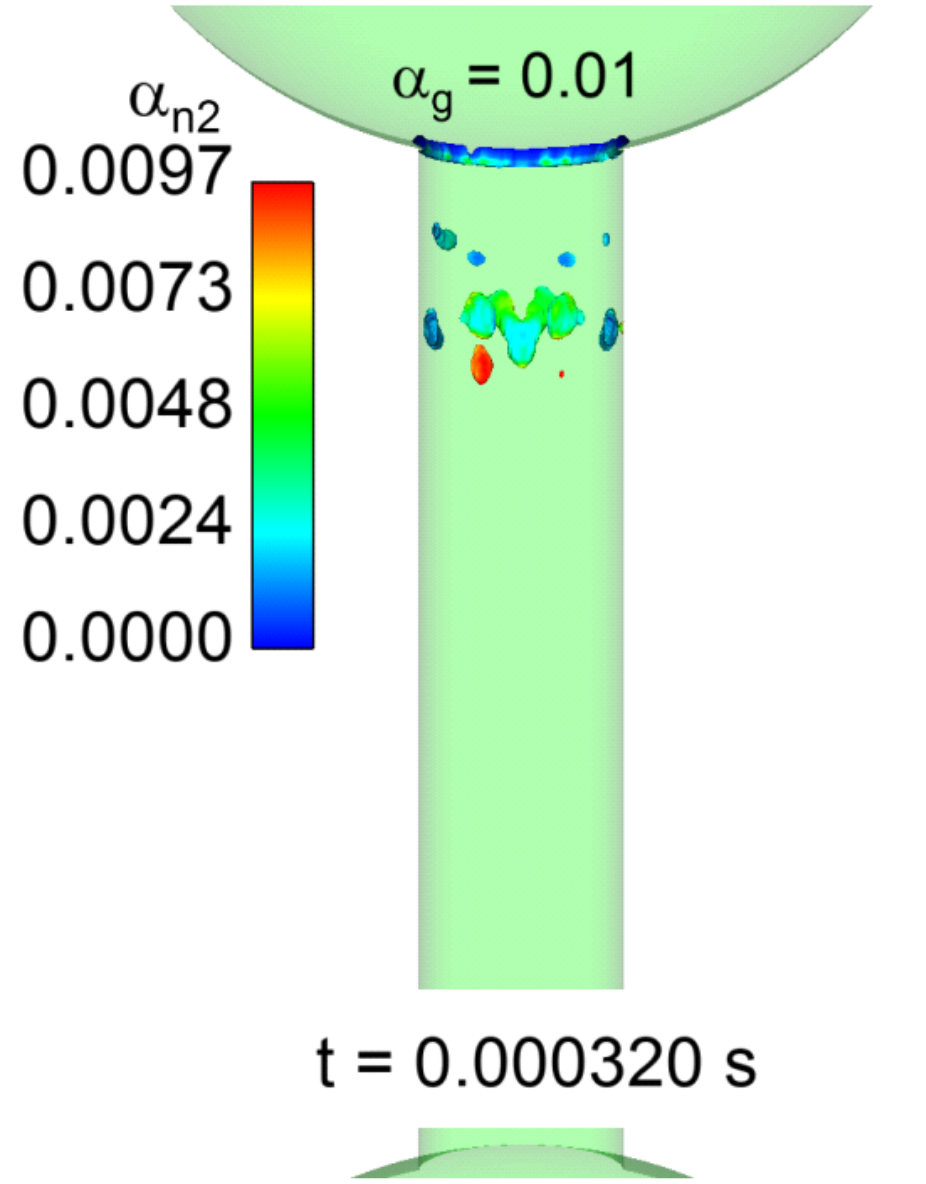
α_{n2}
0.0097
0.0073
0.0048
0.0024
0.0000
α_g = 0.01
t = 0.000320 s

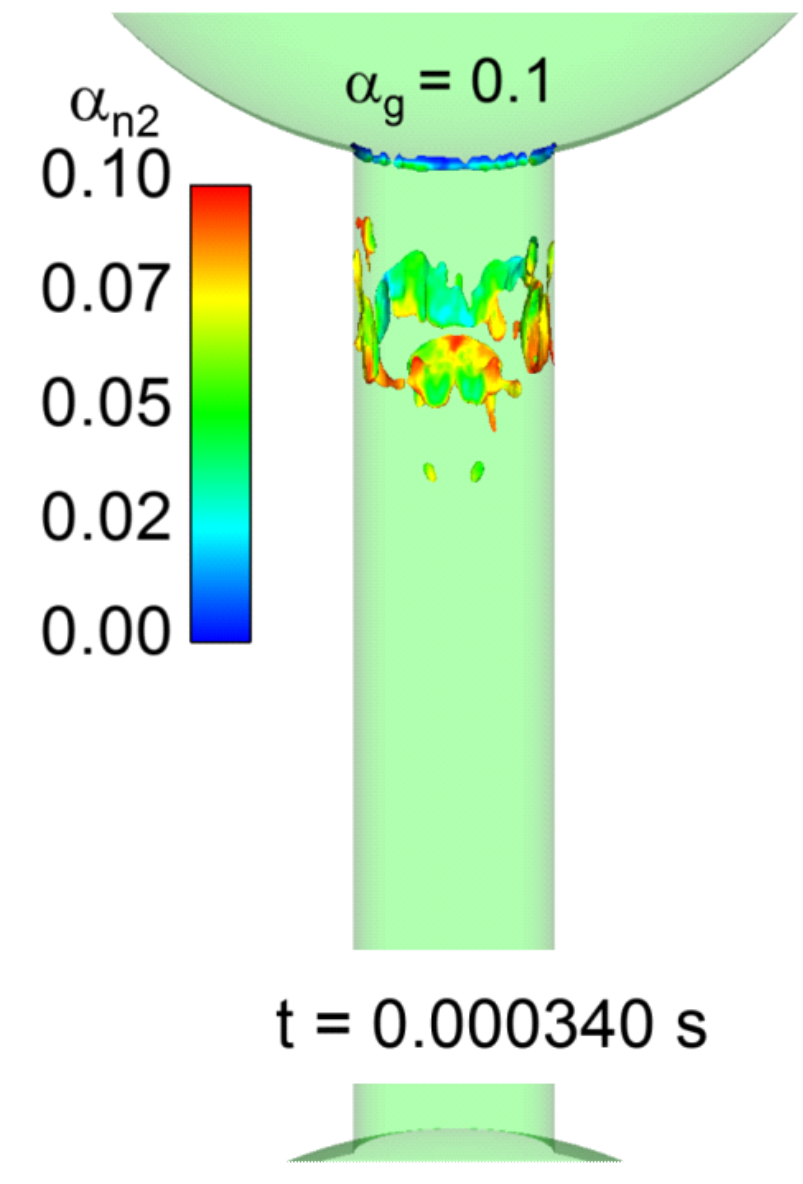
$\alpha_g = 0.1$
α_{n2}
0.10
0.07
0.05
0.02
0.00
t = 0.000340 s

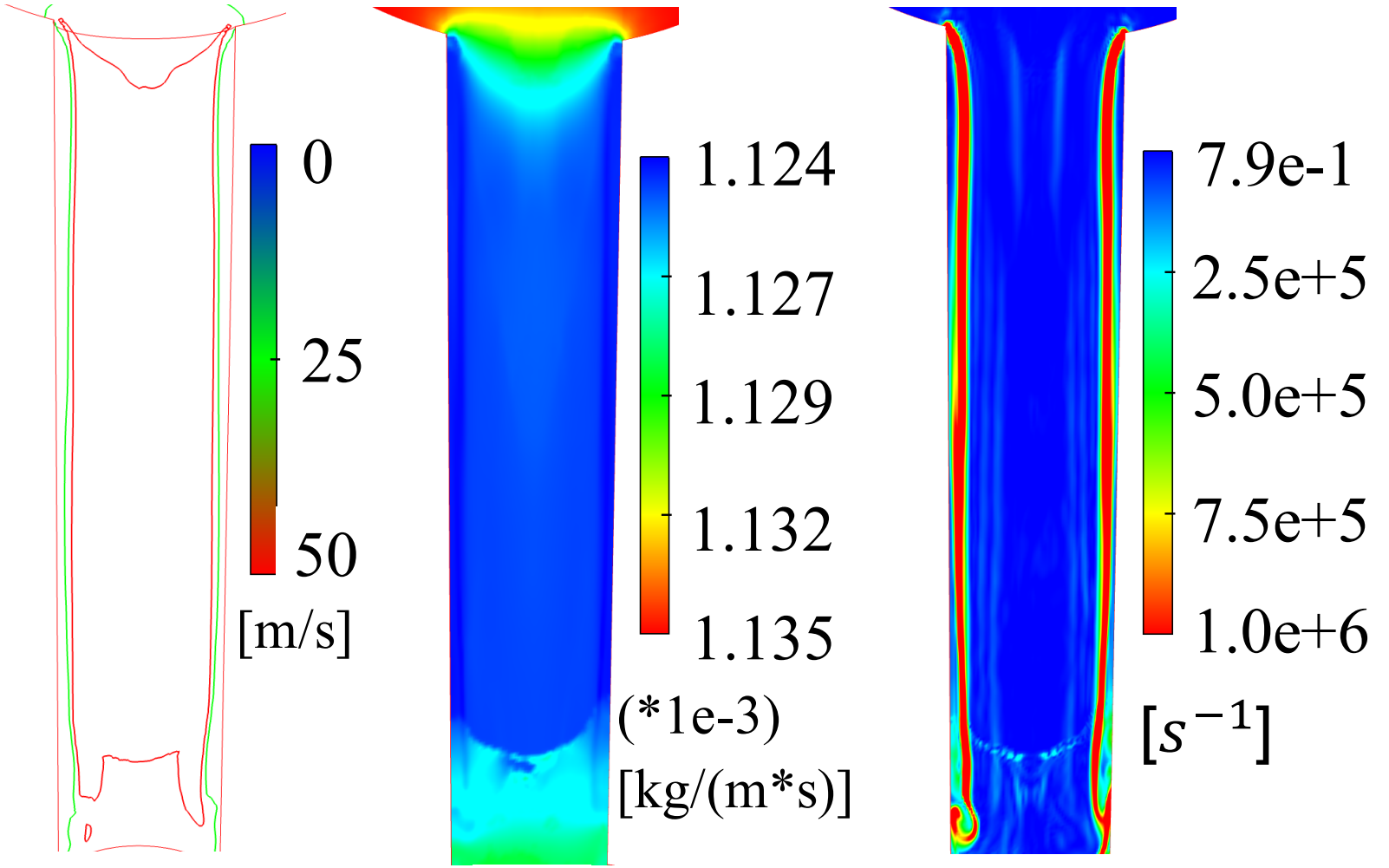

Non-Degassed

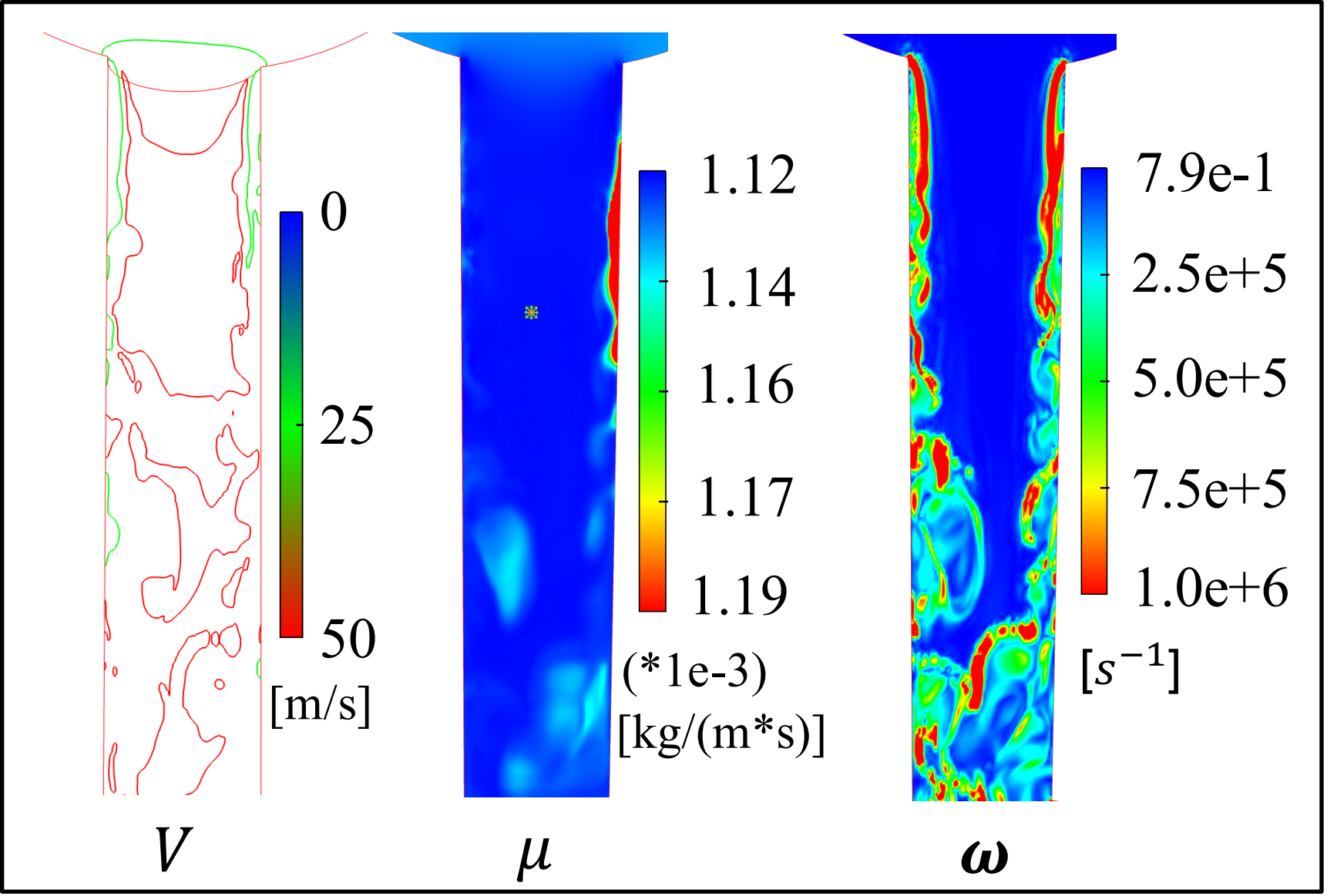
0
25
50
[m/s]
1.12
1.14
1.16
1.17
1.19
(*1e-3)
[kg/(m*s)]
7.9e-1
2.5e+5
5.0e+5
7.5e+5
1.0e+6
[s^{-1}]
V
μ
ω

Degassed

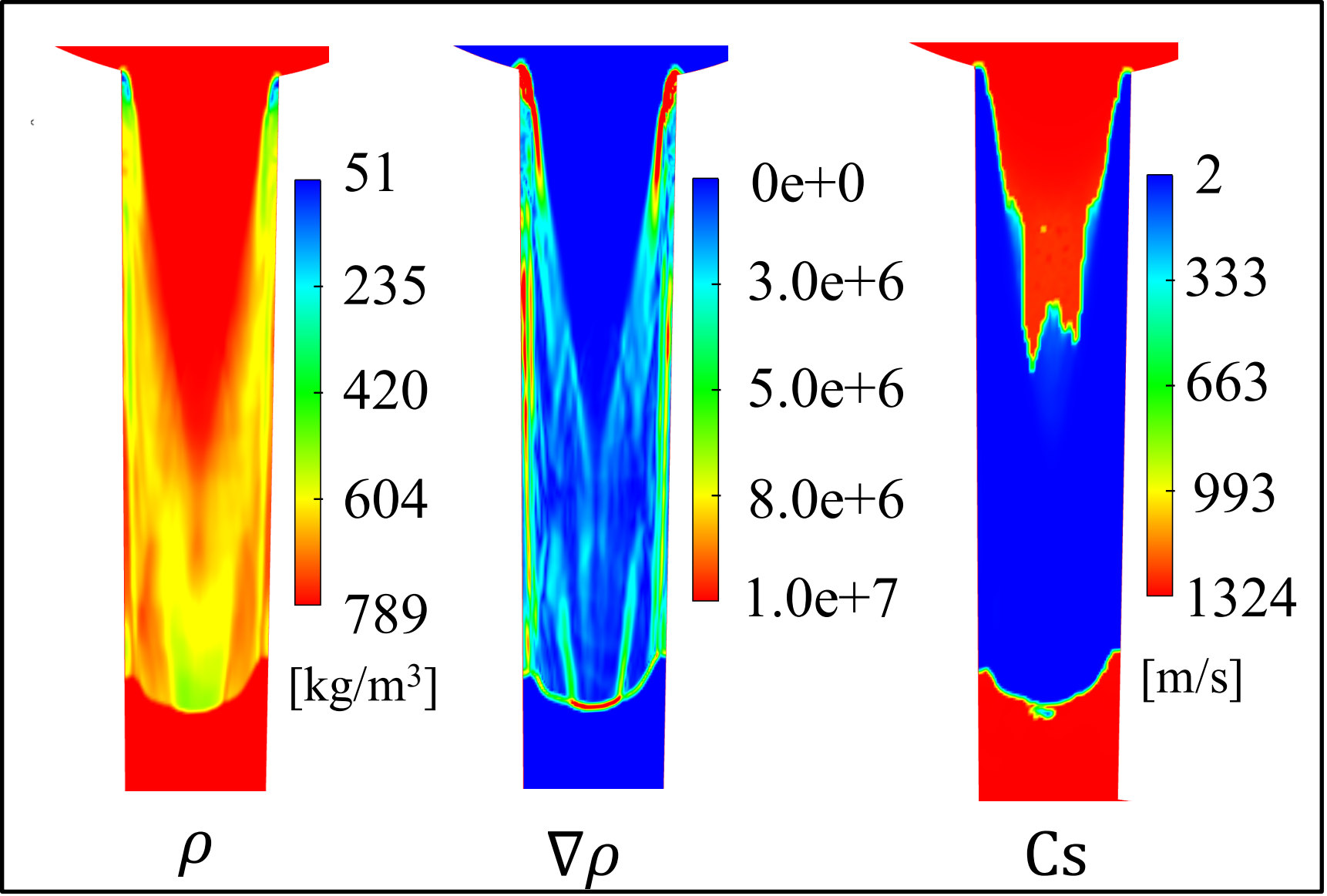

Non-Degassed

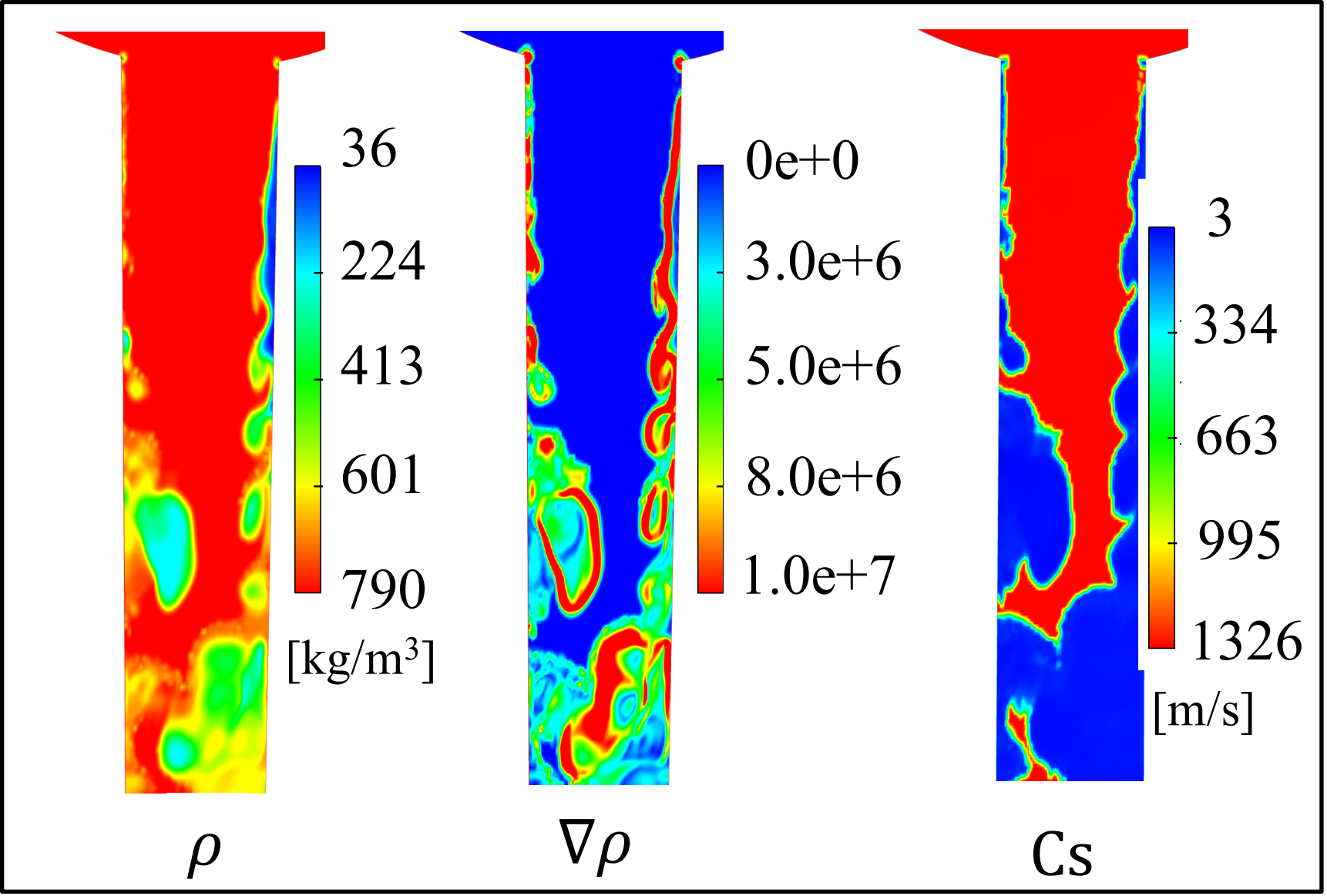
36
224
413
601
790
[kg/m³]
0e+0
3.0e+6
5.0e+6
8.0e+6
1.0e+7
3
334
663
995
1326
[m/s]
ρ
∇ρ
Cs

Degassed

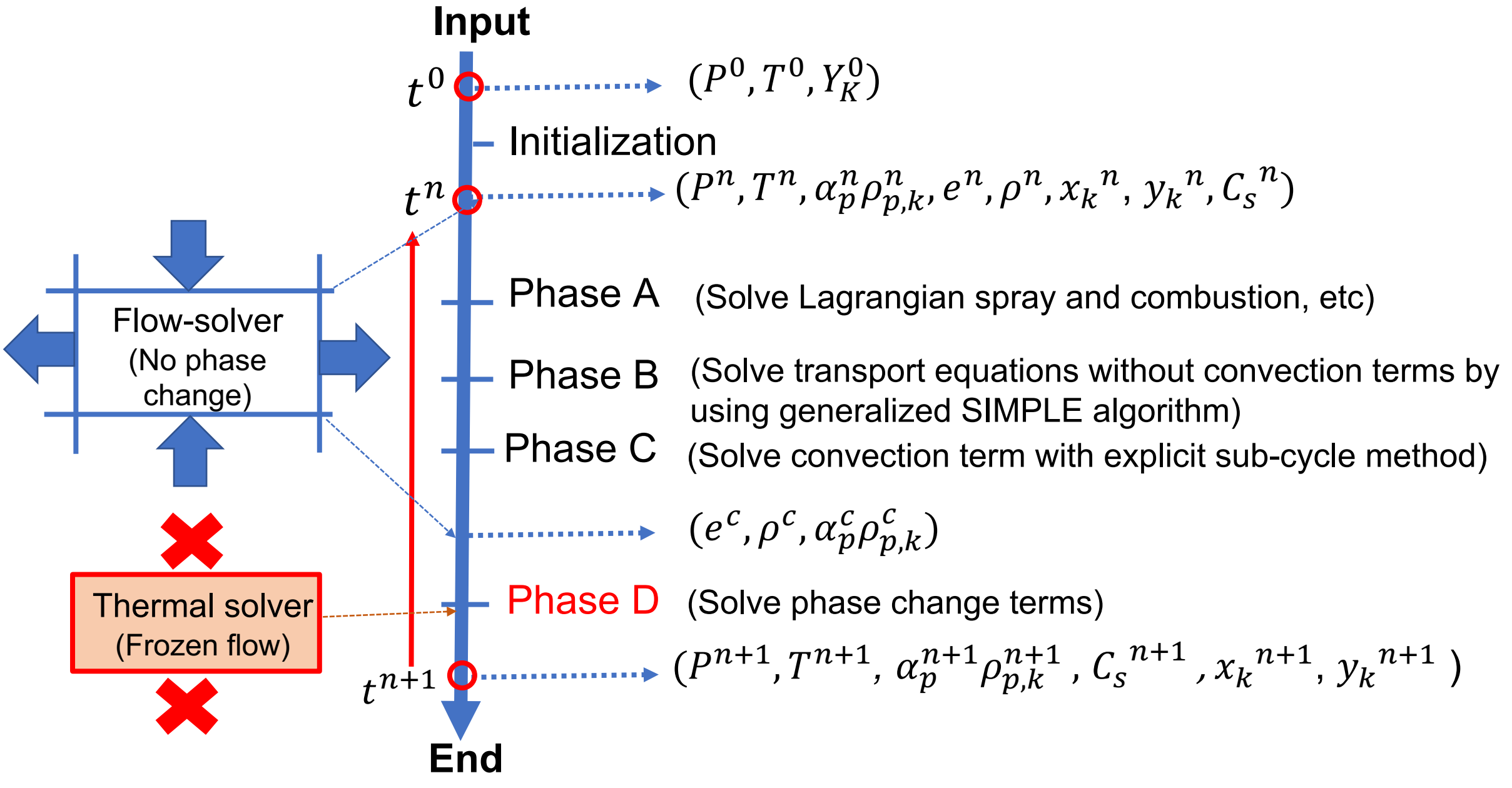
Input
t^0
(P^0, T^0, Y_K^0)
Initialization
t^n
$(P^n, T^n, \alpha_p^n \rho_{p,k}^n, e^n, \rho^n, x_k{}^n, y_k{}^n, C_s{}^n)$
Flow-solver
(No phase change)
Phase A
(Solve Lagrangian spray and combustion, etc)
Phase B
(Solve transport equations without convection terms by using generalized SIMPLE algorithm)
Phase C
(Solve convection term with explicit sub-cycle method)
$(e^c, \rho^c, \alpha_p^c \rho_{p,k}^c)$
Thermal solver
(Frozen flow)
Phase D
(Solve phase change terms)
t^{n+1}
$(P^{n+1}, T^{n+1}, \alpha_p^{n+1} \rho_{p,k}^{n+1}, C_s{}^{n+1}, x_k{}^{n+1}, y_k{}^{n+1})$
End